2

NPS-PH-92-008

NAVAL POSTGRADUATE SCHOOL

Monterey, California

A Self-affine Multi-fractal Wave/ Turbulence Discrimination Method Using Data from Single Point Fast Response Sensors in a Nocturnal Atmospheric Boundary Layer

by

R.F. Kamada and A.J. DeCaria

April 1992

Report for Period
October 1990 - September 1991

Approved for public release; distribution unlimited

Prepared for: U.S. Air Force, Space Division,
Los Angeles AFB, California 90009

NAVAL POSTGRADUATE SCHOOL
Monterey, California

Rear Admiral R. W. West
Superintendent

H. Shull
Provost

The work reported herein was prepared for and funded by U.S. Air Force Space Systems Division, Los Angeles, CA, 90009.

This report was prepared by

Ray Kamada

R. F. KAMADA,
Adjunct Research
Professor of Physics

Reviewed by:

KE Woehler

K. E. Woehler,
Chairman,
Department of Physics

Released by:

P.J. Marto

Paul J. Marto,
Dean of Research

UNCLASSIFIED
SECURITY CLASSIFICATION OF THIS PAGE

REPORT DOCUMENTATION PAGE

Form Approved
OMB No 0704-0188

1a REPORT SECURITY CLASSIFICATION
UNCLASSIFIED

1b RESTRICTIVE MARKINGS

2a SECURITY CLASSIFICATION AUTHORITY

2b DECLASSIFICATION / DOWNGRADING SCHEDULE

3 DISTRIBUTION / AVAILABILITY OF REPORT
Approved for public release;
distribution is unlimited

4 PERFORMING ORGANIZATION REPORT NUMBER(S)
NPS-PH-92-008

5 MONITORING ORGANIZATION REPORT NUMBER(S)

6a NAME OF PERFORMING ORGANIZATION
Naval Postgraduate School

6b OFFICE SYMBOL *(If applicable)*

7a NAME OF MONITORING ORGANIZATION
USAF Space Systems Division

6c. ADDRESS *(City, State, and ZIP Code)*
Monterey, CA 93943-5000

7b ADDRESS *(City, State, and ZIP Code)*
Los Angeles AFB, CA 90009

8a. NAME OF FUNDING / SPONSORING ORGANIZATION
USAF Space Systems Division

8b OFFICE SYMBOL *(If applicable)*
USAF/SSD

9 PROCUREMENT INSTRUMENT IDENTIFICATION NUMBER
MPIR FY76169100412

8c. ADDRESS *(City, State, and ZIP Code)*
Los Angeles AFB, CA 90009

10 SOURCE OF FUNDING NUMBERS

PROGRAM ELEMENT NO	PROJECT NO	TASK NO	WORK UNIT ACCESSION NO

11 TITLE *(Include Security Classification)*
A Self-affine Multi-fractal Wave/Turbulence Discrimination Method Using Data from Single Point Fast Response Sensors in a Nocturnal Atmospheric Boundary Layer

12 PERSONAL AUTHOR(S)
R.F. Kamada

13a TYPE OF REPORT
Technical Report

13b TIME COVERED
FROM 10-90 TO 9-91

14 DATE OF REPORT *(Year, Month, Day)*
April 10, 1992

15 PAGE COUNT
45

16 SUPPLEMENTARY NOTATION

17 COSATI CODES

FIELD	GROUP	SUB-GROUP

18 SUBJECT TERMS *(Continue on reverse if necessary and identify by block number)*
Stable boundary layer, self-affine fractals, turbulence intermittency, coherent structures, wave trains, wave-breaking

19 ABSTRACT *(Continue on reverse if necessary and identify by block number)*

We present D_A, a self-affine, multi-fractal which may become the first routine wave/turbulence discriminant for time series data. Using nocturnal atmospheric data, we show the advantages of D_A over self-similar fractals and standard turbulence measures such as FFTs, Richardson number, Brunt-Väisälä frequency, buoyancy length scale, variances, turbulent kinetic energy, and phase averaging. D_A also shows promise in resolving "wave-break" events. Since it uses local basis functions, D_A may be an ideal tool to detect intermittent turbulence, coherent structures, and discrete wave trains in general. D_A may also be a measure of chaos in general.

20 DISTRIBUTION / AVAILABILITY OF ABSTRACT
☒ UNCLASSIFIED/UNLIMITED ☐ SAME AS RPT ☐ DTIC USERS

21 ABSTRACT SECURITY CLASSIFICATION
UNCLASSIFIED

22a NAME OF RESPONSIBLE INDIVIDUAL
R.F. Kamada

22b TELEPHONE *(Include Area Code)*
(408) 646-2674

22c OFFICE SYMBOL
PH

DD Form 1473, JUN 86 *Previous editions are obsolete* SECURITY CLASSIFICATION OF THIS PAGE

S/N 0102-LF-014-6603 UNCLASSIFIED

I. INTRODUCTION

The second, third, and fourth moments of fluctuation velocity, temperature, and passive tracer concentrations, and their cross correlations have generally been used to estimate the magnitude of dispersive atmospheric transport. This applies to the transport of momentum, energy, humidity, and contaminants such as pollutants. To avoid overestimates of transport, we must also be able to distinguish between wave induced and turbulent contributions to these fluctuation quantities, since periodic wave motion is much less dispersive than aperiodic turbulence. This applies particularly in transitionally turbulent regimes and regions such as the nocturnal atmospheric boundary layer and convective entrainment zone, where the mean flow is punctuated by both intermittent turbulence and waves. However, current algorithms for separating waves from turbulence are either unreliable, not operationally useful, or both. a facile wave/turbulence discriminant has not been demonstrated in the literature.

Here we study D_A, a self-affine, multi-fractal which may be the first operationally useful wave/turbulence discriminant for typical time series data. We discuss and demonstrate its advantages over a self-similar fractal, Fourier transforms, and other standard turbulence measures, such as Richardson number (R_i), Brunt-Väisälä frequency (BVF), buoyancy length scale (l_B), variances, and turbulent kinetic energy (TKE). We also discuss this new method's operational advantages over the phase averaging technique. For the comparisons we use nocturnal data from the 300 meter tower at the Boulder Atmospheric Observatory. We also suggest that D_A be tested as a general measure of the degree of chaos in systems ranging from waves and limit cycles to standard Lorenz, Henon, and Poincare maps, to transitional turbulence, and turbulence displaying an extended inertial subrange.

Fractal self-similarity exists when a geometric feature re-appears at successively smaller scales, where each successive scale is separated by a constant scaling factor (Mandelbrot, 1977). In fluids where turbulence lacks rigid geometric structure, we must instead test the statistical properties describing the ensemble mean geometry of the flow structure for possible self-similarity.

Previous studies have suggested strong potential for a fractal self-similarity approach to wave/turbulence discrimination. Feigenbaum (1980) discovered that low order turbulence, i.e., chaos, in viscousless systems possesses an underlying self-similarity and hence fractally intermittent character. He showed that this self-similarity in the density of Lagrangian particle streamlines appears only when the attractor, the point or area about which the particle motion occurs in real or phase space becomes unstable, i.e., strange. For waves or even limit cycle motion about fixed attractors, self-similarity does not occur. Pertinent to time series analysis, this self-similarity appears in real as well as phase space.

With regard to real viscous fluids, Kamada (1988a,b) showed a length scale self-similarity in atmospheric transitional turbulence for the capping inversion above a convective mixed layer. Sreenivasan and Meneveau (1986), and Presad and Sreenivasan (1990) found that the interfacial convolutions between turbulent and non-turbulent regions of a shear flow are self-similar and thus have a fractal dimension. However, pure self-similarity does not apply across all atmospheric turbulence scales because eddies are increasingly compressed vertically with scale, due to stability. However, Lovejoy and Schertzer (1984) included this compression by using a multi-fractal, self-affine stretch modification to the standard self-similar fractal. Packard et al. (1980) and Pawelzik and Schuster (1987) also studied the fractal dimensions of attractors inferred from a time series.

However, the aim here is to find and utilize the fractal dimension of the time series itself, not the dimension of the phase space attractor or the dimension of the turbulence field in real space. Since a time series is a digital sampling, a time series trace of a fractal process should also show fractal characteristics. For example, Carter et al. (1986) found that the known fractal characteristics of cloud geometry in real space were also evident in the time series of their infrared intensity versus azimuth viewing angle.

In real applications fractal analysis has potential advantages over standard spectral methods. 1) Less data manipulation is required. Standard Fourier transform techniques require that the data be periodic within the data window to avoid the introduction of fictitious high frequency noise. This requires tapering the data within the window so that its endpoints have the same value. This is not required for fractal analysis. 2) Fractal analysis' biggest advantage is that sudden amplitude changes, involving such phenomena as truncated gravity wave trains, breaking Kelvin-Helmholtz instabilities, or turbulent ramp structures pose no problems. In Fourier analyses a linear combination of wave numbers much higher than the time resolution is required to accurately account for such near-discontinuities. This is because the basis functions for standard spectral analysis: sinusoids, Legendre or Leguerre polynomials, Bessel functions, etc., are global, i.e., infinite in length, rather than discrete; whereas fractal analysis naturally assumes a discrete Chapeau (top hat) basis function over the time resolution in question. And this basis function inherently spans the ideal range: from the chosen span of the time series to the available limit of resolution. Therefore, functions involving frequencies shorter than the available resolution are not required to portray large jumps or discontinuities. This suggests that fractal analysis may be quite useful in analyzing discrete, coherent wave trains and intermittent turbulence structures in general.

II. THEORY

A. Current ways to distinguish waves from turbulence

Since linear waves transport no heat, the cross-spectral method assumes for waves that the vertical velocity and temperature exhibit a small cospectrum and large quadrature spectrum, i.e., temperature lags vertical velocity by 90°, while turbulence shows a large cospectrum and small quadrature spectrum. But Finnigan (1988) noted that near-surface gravity waves are non-linear, so the co-spectrum is usually comparable to the quadrature spectrum.

The spectral gap method assumes a wave/turbulence gap in the boundary layer power spectra (Nai-Ping, 1983). Caughey (1977) ties the position of this gap to the Brunt-Väisälä frequency (BVF), which should be the highest frequency of gravity wave that the atmosphere will support. This frequency is often, but not always, lower than turbulence injection scales. Wave phase velocity also adds to the apparent frequency. Thus, spectral gaps in wave number may disappear in the frequency domain for time series from a fixed sensor (Caughey and Readings , 1975).

Phase averaging subtracts the wave and mean components from the signal, leaving turbulence as the remainder (Finnigan, ibid). But one must assume a wave exists and its frequency must accurately estimated *prior* to the analysis. A surface microbarograph array is usually needed to determine wave frequency reliably, but most tower sites lack microbarographs. Problems also arise, if wave amplitudes change greatly with time, if coherence is lost after a few periods, or if non-linear dispersion changes the wave frequency. We suggest that phase averaging is suitable for some aspects of wave/turbulence analysis, but only after wave presence has been established, perhaps most easily by multi-fractal analysis.

The following discusses how multi-fractal analysis can establish such wave presence from single point measurements, without microbarographs, or assumptions about quadrature spectra or spectral gaps.

B. Basic concepts of self-similar fractal dimnesion

For clarity we outline basic fractal concepts before describing the self-affine multi-fractal operator used for this analysis.
The minimum number of boxes of side ε needed to cover a set of points on a two-dimensional plot scales as

$$N(\varepsilon) \approx \frac{F}{\varepsilon^{D}} , \qquad \text{(II.1)}$$

where D is defined as the capacity dimension of the set and F, the lacunity (Mandelbrot, 1977). If the set forms a straight line, then D = 1 because, if the box length is halved, twice as many boxes are needed to cover the line. If the set consists of uniformly distributed points in a plane, then D = 2, since four times as many boxes are needed.

If the points are not uniformly distributed, then D can be non-integer. The set of points is then fractal with dimension D, defined in the limit as ε approaches zero. This definition is called the box dimension, D_B, (Mandelbrot, 1985), and is given as

$$D_B = \lim_{\varepsilon \to 0} \frac{\log N(\varepsilon)}{\log \frac{1}{\varepsilon}} \ . \qquad \textbf{(II.2)}$$

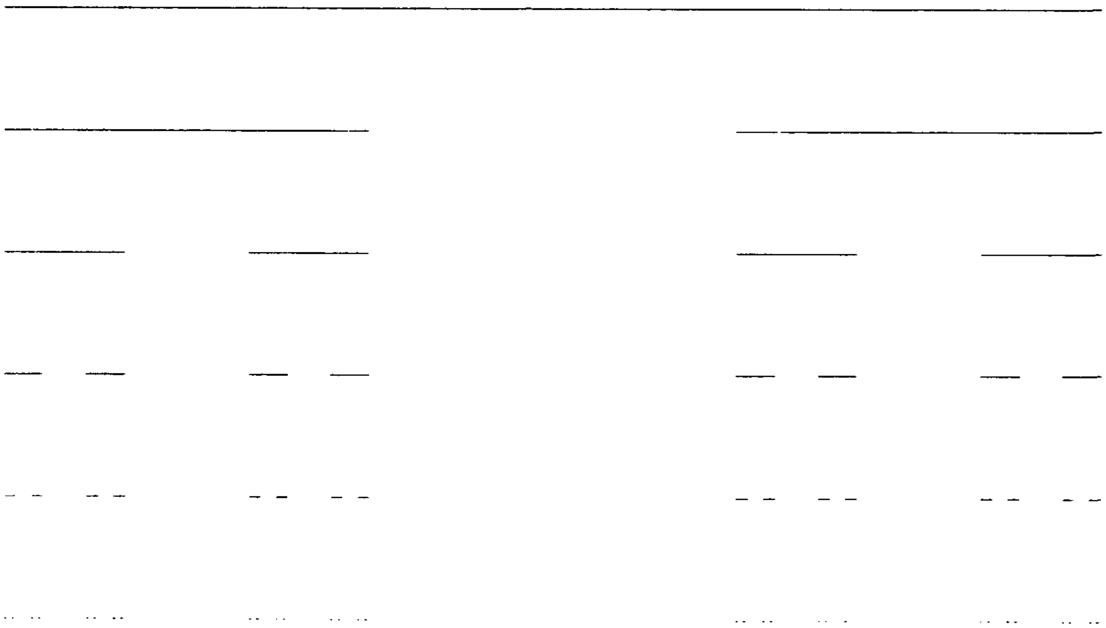

Figure 1 - Construction of the Cantor set.

The Cantor set in fig. 1 has a non-integer D_B. It is formed by removing the middle third of a line segment, removing the middle third of each remaining segment, and re-iterating to infinity. The set is self-similar because the geometric structure seen at the largest scale re-appears for all smaller scales removed by successive factors of three. For an initial unit length, N(1)=1 box of side $\varepsilon = 1$ is needed to cover the set. For $\varepsilon=1/3$, N(1/3)=2, and for $\varepsilon=1/9$, N(1/9)=4. Thus, ε is generally 3^{-n}, and $N(\varepsilon)$ is 2^n, where n = 0,1,2,3,...,∞ (Grebogi et al., 1987). Noting that $n\to\infty$ implies $\varepsilon\to 0$, from eqn. II.2, D_B for the Cantor set becomes intermediate between a point ($D_B = 0$) and a line ($D_B = 1$). That is,

$$D_B = \lim_{n\to\infty} \frac{\log 2^n}{\log 3^n} = \frac{\log 2}{\log 3} = 0.63092... \qquad \textbf{(II.3)}$$

Unlike the analytic Cantor set, D_B must be evaluated numerically for most fractal sets. This is done by removing the limit in II.2 and reordering terms to get

$$\log N(\varepsilon) = \log F - D_B \log \varepsilon \ . \qquad \textbf{(II.4)}$$

Then $-D_B$ is the slope of the plot of log $N(\varepsilon)$ vs. log ε, and log F is the y-intercept.

In practice, real time series will contain some noise, so $L(\varepsilon)$ will not be exact. Thus, multiple values of ε should be used, and some form of regression employed to find the slope (see section III). Moreover, the data may only be fractal over a certain range, so the choice of inner and outer scales, ε_o and ε_i, over which the slope is determined may be narrower than those defined by purely objective limits.

Digitized data imposes an objective limit on ε_i because the curve shape between discrete data points is unknown, so it is simplest to assume a straight line. As before, one plots log $N(\varepsilon)$ vs $\log\varepsilon$ to find D_B. For $\varepsilon < \varepsilon_m$ the curve scales as a one dimensional line, the assumed shape between adjacent data points. So the inner scale of resolution, ε_i, must span at least three data points, i.e., $2\varepsilon_m$. This value happens to be same as the Nykqvist cutoff for Fourier spectra, but for different reasons.

An objective criterion also exists for the choice of outer scale, ε_o, when the time series contains waves. As shown in fig. 2 for a single sinusoid, log $L(\varepsilon)$ versus log ε shows nearly zero slope for $\varepsilon < \lambda/3$, whereas for ε slightly greater than $\lambda/3$ the plot is nearly vertical. So we suggest for wave containing time series that $\varepsilon_o \leq \lambda_m/3$, where λ_m is the foreseen minimum wave period.

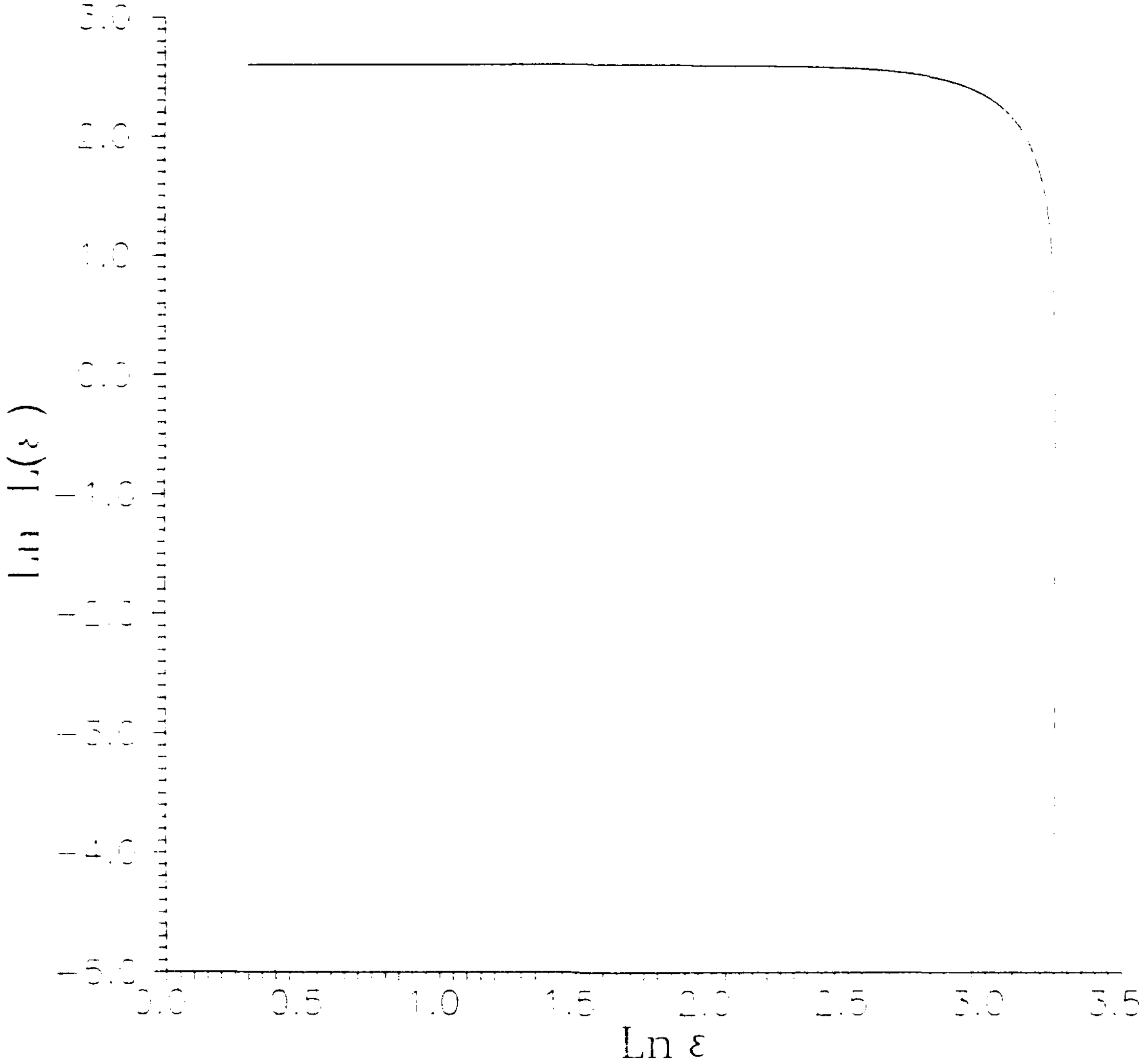

Figure 2 - Self-affine L(ε) for 1800 point sinusoid.

Mandelbrot (1977) describes another way to determine fractal dimension for a continuous curve in two dimensions, such as a geographical coastline. Here, curve length is defined as

$$L(\varepsilon) \approx \varepsilon N(\varepsilon) \ , \tag{II.5}$$

where $N(\varepsilon)$ is given as

$$N(\varepsilon) = \frac{F}{\varepsilon^D} \ , \tag{II.6}$$

and F is again the lacunity.

Lacunity measures the length of one fractally scaling curve to another of the same D. I.e., assume that within the limits, ε_0 to ε_i the fractal dimension is constant for any segment of a real curve of finite length. Then for any two segments of unequal length, II.6 shows that the step length ratio will be

$$\frac{N_1(\varepsilon)}{N_2(\varepsilon)} = \frac{\frac{F_1}{\varepsilon^D}}{\frac{F_2}{\varepsilon^D}} = \frac{F_1}{F_2} \ . \tag{II.7}$$

Using II.6 in II.5, $L(\varepsilon)$ can be written as

$$L(\varepsilon) \approx F\varepsilon^{1-D} \ . \tag{II.8}$$

Taking the log of II.8 yields the straight line equation,

$$\log L(\varepsilon) = \log F + (1-D)\log\varepsilon \ . \tag{II.9}$$

The slope of log $L(\varepsilon)$ by log ε yields (1 - D). To find D first find $L(\varepsilon_0)$. Then, from II.9, log $L(\varepsilon_0)$ = log F + (1-D) logε_0. Now with $L(\varepsilon_i)$, log $L(\varepsilon_i)$ = log F + (1-D)logε_i. This yields two equations in two unknowns, D and F, so in principle

$$D = \frac{\log[\frac{L(\varepsilon_o)}{L(\varepsilon_i)}]}{\log[\frac{\varepsilon_o}{\varepsilon_i}]} \ . \tag{II.10}$$

This procedure amounts to spanning the curve with circles of diameter ε. So $L(\varepsilon)$ is also the minimum number of circles of diameter ε required to cover the curve times their diameter. Thus, $L(\varepsilon)$ can be measured by stepping along the curve with a compass whose span is set to ε. Mandelbrot (1985) terms this estimate the "compass dimension", D_C.

To show that D_C is equivalent to D_B, solve II.8 for D to get

$$D = \frac{\log L(\varepsilon) - \log(F)}{\log\frac{1}{\varepsilon}} + 1 \ . \qquad \textbf{(II.11)}$$

Substituting $L(\varepsilon)$ from II.5 gives

$$D = \frac{\log N(\varepsilon) - \log(F)}{\log\frac{1}{\varepsilon}} \ , \qquad \textbf{(II.12)}$$

and in the limit as $\varepsilon \to 0$, since $N(\varepsilon)$ is much larger than F, this yields

$$D = \lim_{\varepsilon \to 0} \frac{\log N(\varepsilon)}{\log\frac{1}{\varepsilon}} \ , \qquad \textbf{(II.13)}$$

which is D_B.

In essence fractal dimension is a measure of the jaggedness or degree of convolution of a curve given in terms of the power law dependence of the curve length as a function of resolution.

The box method divides the data plane into discrete boxes of length, ε, where $N(\varepsilon)$ is the number of boxes having at least one point on the curve. So, for D_B every box in the domain must be checked, even though most boxes are empty, while D_C considers only the circles covering points on the curve. So though D_C and D_B are identical, D_C is faster to compute.

C. Time series applications

Unlike coastlines, a time series plot has axes with different units of measure, time versus amplitude. This poses a problem, since the "length" of a time series trace cannot be measured without specifying an arbitrary scaling ratio between axis units. I.e., different ratios will give different values of D_C. Thus, though calculable, Mandelbrot (1985) suggests that D_C may not be meaningful for time series analysis, since its value can even exceed two, if the y to x-axis scaling ratio is large enough. This warrants exploring a shift in approach to measuring fractal dimension, which we describe as follows.

McHardy and Czerny (1987) applied a "self-affine", "multi-fractal" operator to their time series data. Meaning "in the same way", self-affinity requires that one axis be stretched or compressed at each successive resolution by the same constant factor with respect to the other axis. Thus, McHardy and Czerny defined their self-affine "length metric" as

$$L(\varepsilon) = \frac{1}{\varepsilon}\int_0^T |F(t+\varepsilon) - F(t)|\,dt\ , \qquad \textbf{(II.14)}$$

where now the abscissa scaling changes by the factor, $\varepsilon_n/\varepsilon_{n+1}$, each time ε changes by the factor $\varepsilon_{n+1}/\varepsilon_n$ (their length metric differs from the standard self-affine length metric, which uses the integrand, $([F(t+\varepsilon)-F(t)]^2 + \varepsilon^2)^{1/2}$). This new metric leads to,

$$D = -\frac{d\log L(\varepsilon)}{d\log\varepsilon}\ . \qquad \textbf{(II.15)}$$

$L(\varepsilon)$ from II.14 will be much longer at small ε, but note that D in II.15 is defined as the change rate of log length with log resolution, not the ratio of log length to log resolution. Since time, ε, cancels in the length metric, $L(\varepsilon)$ only has units of amplitude. This avoids arbitrary ratios between amplitude and time units and makes the problem one dimensional, so D is less than unity. Thus, eqn. II.14 presents a natural choice for evaluating time series. Hereafter, we refer to D from this method as D_A.

$L(\varepsilon)$ calculated from II.14 will contain some noise contribution, which is statistically independent of the signal. If its level is known, we can estimate its contribution to $L(\varepsilon)$ by the formula, $L^2_{observed} = L^2_{signal} + L^2_{noise}$. White noise has $D_A = 1$, so it tends to increase the fractal dimension of the time series.

D. Relevant gravity wave and turbulence characteristics.

Gravity waves in the stable boundary layer can be generated by a number of mechanisms, among them: wind shear (Kelvin-Helmholtz instability), storm impulses, and flow over an obstacle. Their amplitudes can vary from a few centimeters to hundreds of meters, with periods from less than a minute up to 40 minutes (Stull, 1988). Wave generation due to flow over an obstacle is significant here. Hunt (1980) gives the natural wavelength of flow over a hill as

$$\lambda = 2\pi U_o/\mathrm{BVF}\ , \qquad \textbf{(II.16)}$$

where U_0 is mean wind speed. The hill "length" is given as L_l, the horizontal distance across the hill at half its maximum elevation. If $\lambda \sim 5L_l$ then lee waves may occur with λ. Moreover, if $\varepsilon \sim 2L_l$, then strong lee waves are possible. Observational studies such as

Caughey and Readings (ibid), Caughey (ibid), and Nai-Ping (ibid), suggest that waves and turbulence commonly coexist in the nocturnal boundary layer, and turbulence generation can sometimes depend on the wave. The idea that gravity waves transfer energy to Kelvin-Helmholtz waves which then "break" is widely used as a model for turbulence generation by waves (Stull, ibid; Atlas et al., 1970), though this model is not universally accepted (Hines, 1988).

Finnigan (ibid) resolved the wave and turbulent portions of the total kinetic energy by phase averaging, and showed horizontal TKE developing in the first quarter wave cycle, while vertical TKE arose during the ensuing third of the cycle. Both components transferred energy from the wave to turbulence. They noted that the wave seemed to modulate the turbulence, but the presence of the turbulence had no apparent effect on the wave.

Gossard et al. (1985) suggest a generation mechanism for boundary layer turbulence where local gradients of θ, u, and v increase steadily, while turbulence decreases. Vertical shear eventually reaches an insupportable value of local Richardson number, leading to growth of local Kelvin-Helmholtz instabilities which grow into turbulence. These various proposals for turbulence initiation and wave/turbulence energy transfer are discussed in the context of our fractal analysis in section IV.

III. METHODS

A. Data

The Boulder Atmospheric Observatory (BAO) (Kaimal and Gaynor, 1983) supplied the data for this study. Data samples included eight levels at: 10, 22, 50, 100, 150, 200, 250, and 300 meters, of:

1. u, v, and w velocity components sampled at 10 Hz by sonic anemometers.
2. wind direction and speed at 1 Hz by propeller vane anemometers.
3. temperature at 10 Hz by platinum wire thermometers, and at 1 Hz by quartz thermometers.

The 1 Hz data were given only as 10 second averages. The 10 Hz data were given at both 10 Hz and as 10 second averages. Noise levels were ≤ .01 °C for the platinum wire thermometer, and ≤ .03 m s^{-1} for the sonic anemometers (J. Gaynor, personal communication).

The data and FORTRAN input read programs were sent on 9 track tape by John Gaynor and Dave Welch of the NOAA Wave Propagation Laboratory. The programs were run on a NPS Computer Science Department Sun4 workstation, with analysis on the NPS mainframe. The data covered three (MST) time periods: A) 2340 9/7/83 - 0340 9/8/83; B) 0440 - 0620 9/9/83; and C) 0000 - 0620 9/19/86.

The temperature time series seemed the least noisy of the available data. So 10 Hz temperature data were plotted at levels four and five (100 and 150 meters) for all three periods. A "wave" was apparent on visual scanning period A at level four, between 0040 and 0105 MST, September 8, 1983 (see fig.3, windows 21-27).

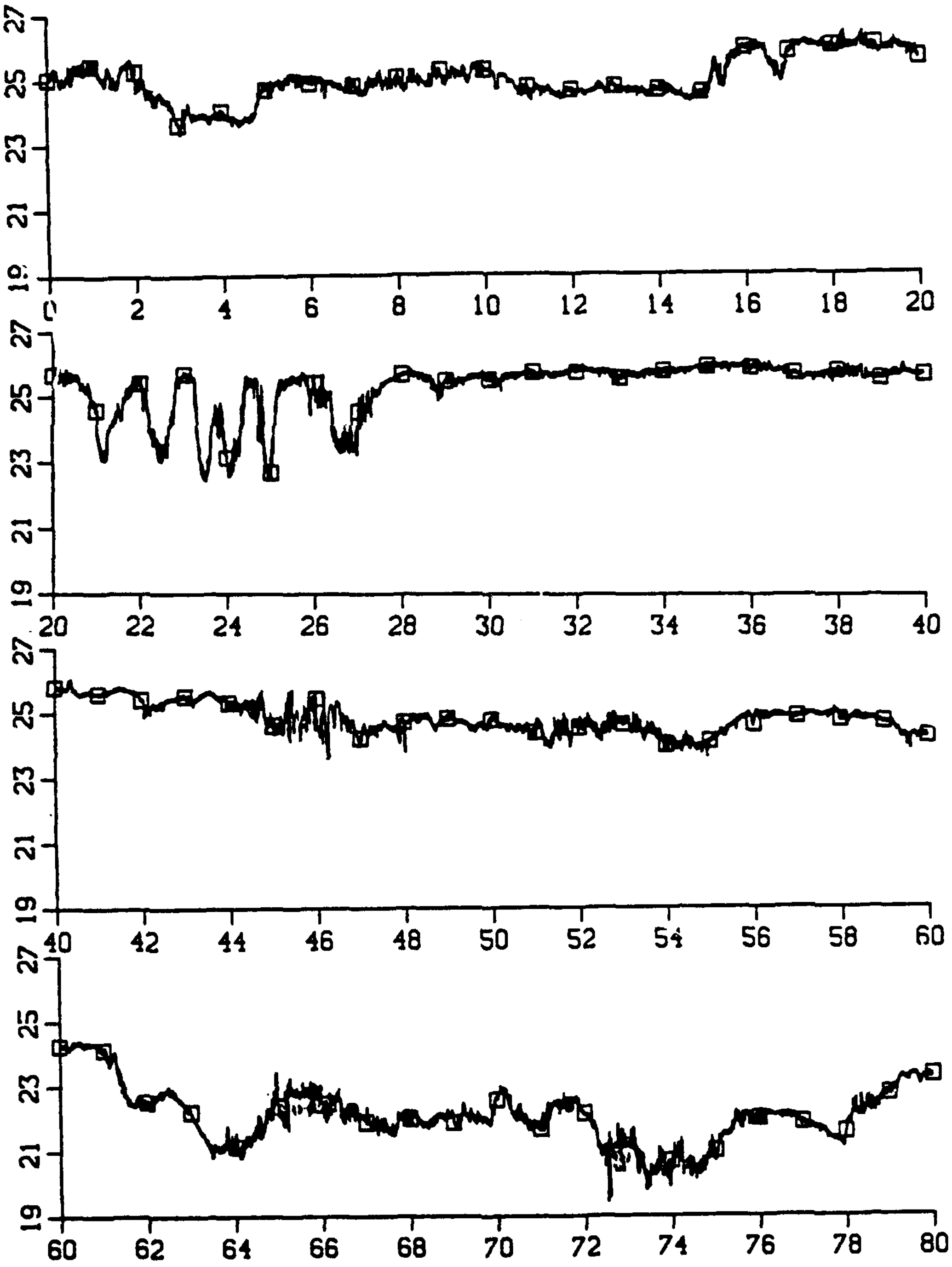

Figure 3 - Temperature (°C) vs. three minute windows. The wave occurs in windows 21 - 27; turbulence episodes in windows 45 - 47, 66 - 67, and 73 - 75.

Since winds were southerly throughout, the "wave" was consistent with the above lee wave criteria and flow over a small hill south of the tower. I.e., eqn. II.16 gave $\lambda \approx 1900$ meters, for an observed BVF ≈ 0.03 Hz, and $U_o = 9$ m s^{-1}. From a USGS map for the 120 ft hill (elev. 5280 ft MSL), $L_l \approx 300$ meters along the tower direction; so $5L_l \approx 1500$ meters. This fits the condition $\lambda \sim 5L_l$. But before and after the "wave" period, the BVF dropped below 0.01 Hz, so λ exceeded 6200 meters, well beyond the lee wave condition. This account is consistent with terrain induction of the wave. Lee wave conditions were approached for windows 43-53, and 61-66, but not as closely, and waves were also not evident in the time series. Other periods showed no clear wave evidence. Period C also showed pronounced noise spikes at 20 minute intervals and high noise levels throughout most of its length.

In period A a reduced temperature variance region followed the "wave" episode. This let us compare fractal characteristics of both "wave" and non-wave portions of the time series. Thus, we focused on level four data from period A for this study.

B. Analysis measures

D_C, D_A, turbulent kinetic energy (TKE) and its component velocity variances, bulk Richardson number (R_B), Brunt-Väisälä frequency (BVF), buoyancy length (l_B), and fast fourier transform (FFT) spectra were all tested as analysis tools on the u, v, w, and T time series at level four. R_B, BVF, and l_B are bulk measures, and were taken across levels three to five, a vertical span of 100 meters. The above parameters were checked for possible correlation with D_A.

The main disadvantage of bulk measures is that they apply to the entire layer rather than a local sensor; D_C, D_A, TKE, FFT spectra, and variance are taken from local values valid only at the sensor. So if an eddy is smaller than the 100 meter layer thickness, it may impact the local sensor but not the heights at which the bulk gradients of U, V, and θ are measured.

D_C was computed for the level 4, 10 Hz temperatures for adjacent three minute windows throughout period A. Three minute windows were chosen, since the "wave" had a period of about 200 seconds. As discussed above, ε_i was set to three data points (.2 sec). ε_o was set to the window length, 1800 data points, for the first run. For all runs the time axis was expanded by a factor of 100, so that .1 seconds on the ordinate was equal to .01°C on the abscissa.

The first run for D_C showed that the curve scaled linearly (slope on the log-log plots was zero) for all $\log \varepsilon \geq 2.25$, or $\varepsilon > 17.8$ seconds for all windows. For most windows, the linearly scaling portion began above $\varepsilon \geq 3.2$ seconds. For better resolution on the fractal part of the curve, the run was repeated with an $\varepsilon_o = 17.8$ seconds. Figure 4 shows a typical plot from this run.

The steep, linear part of the curve was linearly regressed to get D_C. The linear region varied from window to window, depending on the outer scale. ε_0 was determined manually for each window, according to the following procedure.

1. A line was drawn with a straight edge along the steep, linear portion of the curve (point A in Fig. 5).
2. A second line was drawn along the shallow, trailing edge of the curve at high values of log ε.
3. The ordinate where these two lines intersected was taken to be the outer scale, ε_0.

Some windows also required that ε_i, be determined manually in a similar fashion.

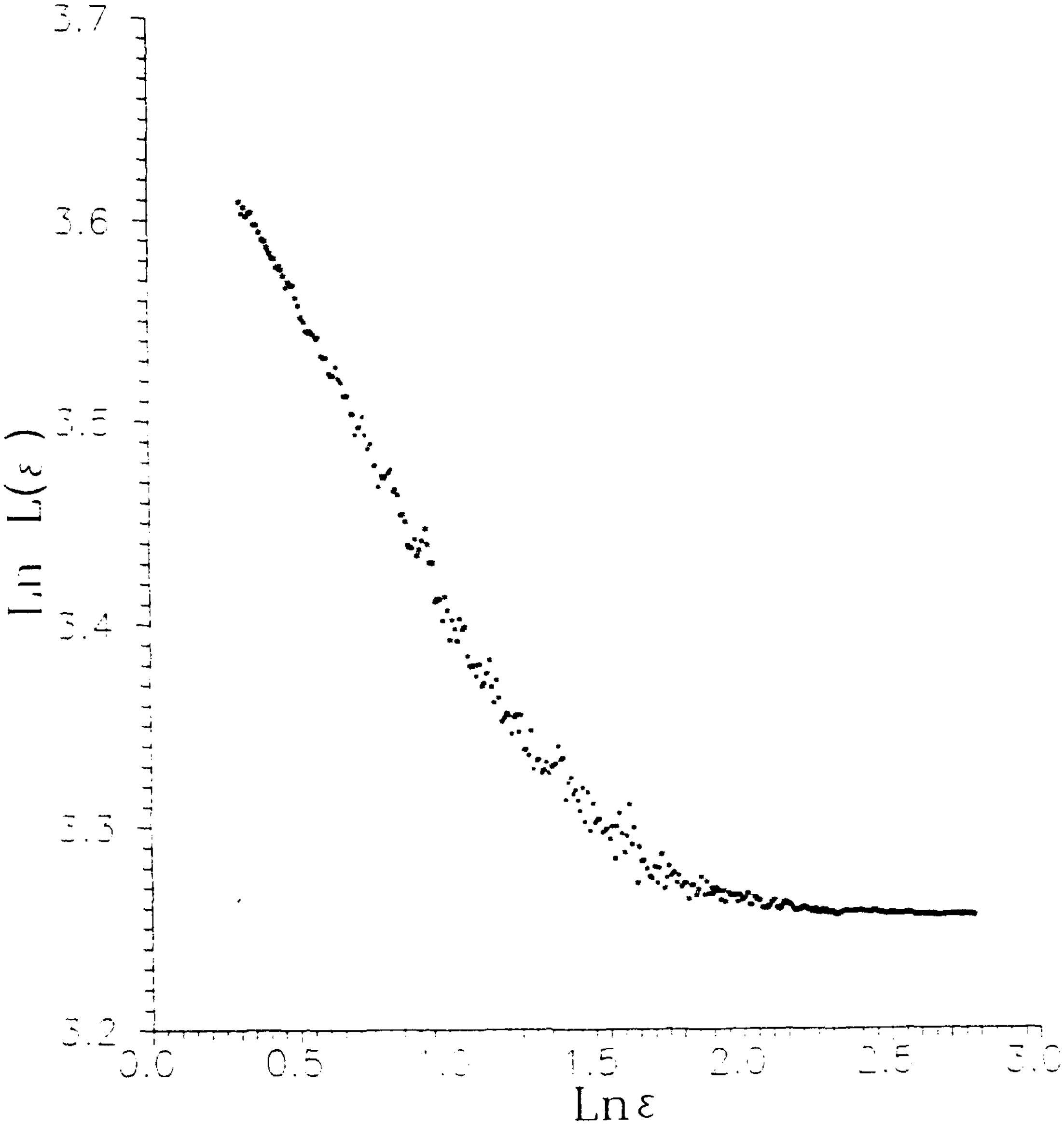

Figure 4 - Typical log-log plot from self-similar algorithm (D_C) from the temperature time series.

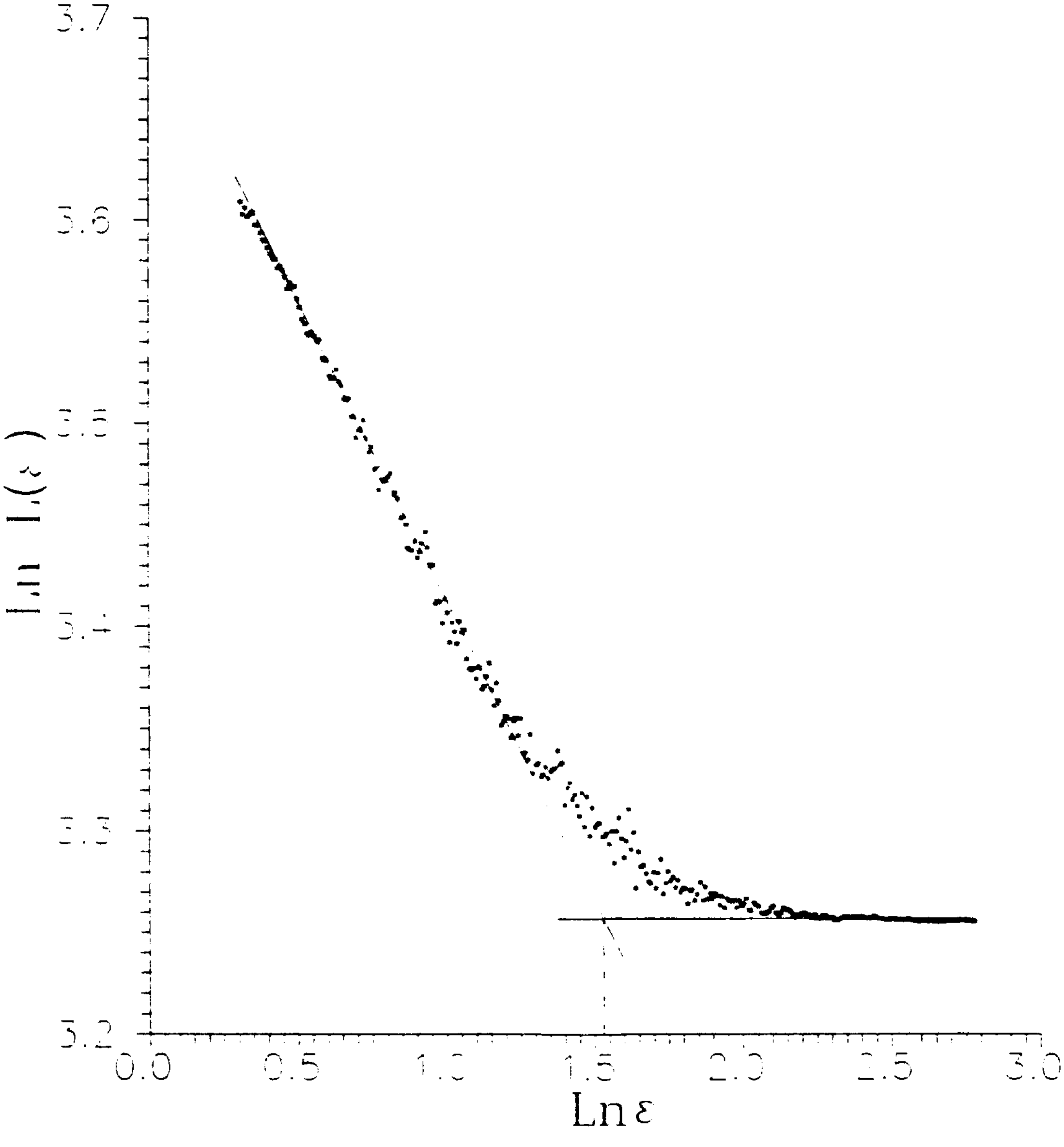

Figure 5 - Determination of largest ε to use in calculating slope for D_C.

D_A was also computed for the temperature and the three velocity components, using the same three minute windows for Period A. ε_i and ε_o were again .2 and 180 seconds for the first run. This allowed approximately three decades of dynamic range.

The first run showed for all windows that log L(ε) vs. log ε had constant, non-zero slope for ε from .2 to around 60 seconds, but not beyond this time duration. Thus, only log $\varepsilon \leq 2.75$ ($\varepsilon \approx 600$) was used, since this still provided a satisfactory 2.5 decades of dynamic range. As mentioned above, another reason for setting $\varepsilon_o = 600$ is that $\lambda_m/3 \approx 600$ for the apparent "wave" period. Thus, unlike D_C, objective criteria could be used to determine the inner and outer scale cutoffs for the slopes. Again a simple linear regression was used to get D_A for each window.

Mean turbulent kinetic energy (TKE) is defined as $\frac{1}{2}(\sigma_u^2 + \sigma_v^2 + \sigma_w^2)$, where σ_u, σ_v, and σ_w are the respective standard deviations of u, v, and w. Variances are often measured over 30 minute to one hour periods because the apparent "spectral gap" often occurs at about 1 hour and allows a convenient separation between large and small scales. Statistical confidence in the value of second moments such as variance also may not reach appropriate levels without averaging over tens of minutes. In our case such a long averaging time would not be useful in determining small scale differences between waves and true turbulence. Instead, the TKE and variances were calculated over the same three minute intervals as D_C and D_A for purposes of direct comparison. All other parameters such as bulk Richardson number or Brunt-Väisälä frequency were also calculated over three minute windows.

Bulk Richardson number, R_B, was checked for possible correlations with D_C or D_A. Ideally, R_f, the flux Richardson number, or R_i, the gradient Richardson number, should be used, since our interest is in the local stability at the sensor. Both R_f and R_i require that the local vertical gradient of the mean wind be known, but this was not available, since the sensors were spaced 50 meters apart vertically. So, instead we used the bulk Richardson number,

$$R_B \equiv \frac{g \, \Delta\overline{\theta}_v \, \Delta z}{\overline{\theta}_v \, [(\Delta\overline{U})^2 + (\Delta\overline{V})^2]} ,$$

where Δ represents the quantity difference between the bottom and top of the layer. The layer thickness, Δz, was 100 meters, with the layer centered on the level of interest.

The virtual potential temperature, θ_v, was assumed equal to potential temperature, θ. Though Stull (ibid) emphasizes that θ_v can differ from θ by up to 4°C, this will not seriously affect R_B for three reasons. First, $\partial\theta_v/\partial z$ will not differ much by substituting θ for θ_v; second, a 4°C difference in the denominator will not change R_B by more than 10 percent; and third, the absolute value of R_B is not important. In this study R_B is only qualitatively important as an indicator of stability changes.

The Brunt-Väisälä frequency, BVF, was chosen to measure static stability and, like R_B, possible correlations with D_C or D_A were tested. BVF is defined as

$$\mathrm{BVF} = \sqrt{\frac{g}{\theta_v}\frac{\partial \theta_v}{\partial z}}\ .$$

As with R_B, we assumed that $\partial\theta_v/\partial z \approx \Delta\theta/\Delta z$ because we wished to explore correlations in temporal changes in BVF with other parameters and were not interested in the actual BVF values.

l_B, the buoyancy length scale, was also determined as the standard deviation of the vertical velocity divided by the Brunt-Väisälä frequency ($l_B = \sigma_w/\mathrm{BVF}$), and was assumed to be a measure of the dominant eddy scale.

Detrended FFT spectra were also computed using a cosine squared, or Hamming window to excise ringing and high frequency noise.

IV. RESULTS AND DISCUSSION

A. Comparisons with local measures

Figure 3, the temperature series, shows both "turbulence" and "wave" episodes. Using three minute windows, Figure 6a shows distinct temperature variance, σ_T^2, peaks. The largest occurs in windows 21-28, cotaneous with the "wave". Three other window periods: 45-47, 64-67, and 73-75 are cotaneous with "turbulence". The other σ_T^2 peaks, like window 62, were cotaneous with monotonic temperature changes across the window which did not seem to be associated with the "wave" or "turbulence". These are absent in the σ_v^2 and σ_w^2 plots (figs. 6b, c), but do appear in σ_u^2 (fig. 6d). Figure 7 shows a TKE spike during the "wave", but also for the three "turbulent" episodes. So the TKE and variances do not seem to distinguish between "wave" and "turbulence"; all appear as local maxima.

For D_A fig. 8 shows a typical log $L(\varepsilon)$ versus log ε plot for a three minute temperature window. Most plots were quite linear for 2.5 decades on the ordinate, from $\varepsilon = .2$ to 60 sec. Figure 9 shows the temperature D_A. Unlike variance, the lowest values occur in windows 21-28 during the "wave". Three other local minima occur in windows: 42, 63, and 78, cotaneous with periods of seemingly low "turbulence" in the time series. Unlike the extended "wave" period, the other local minima occurred only in isolated individual windows.

Figure 10 compares the temperature and velocity D_A. The curves agree, with near-simultaneous minima and maxima on all plots. Figure 11 shows scatter plots of D_A from one time series versus another, indicating good linear correlation.

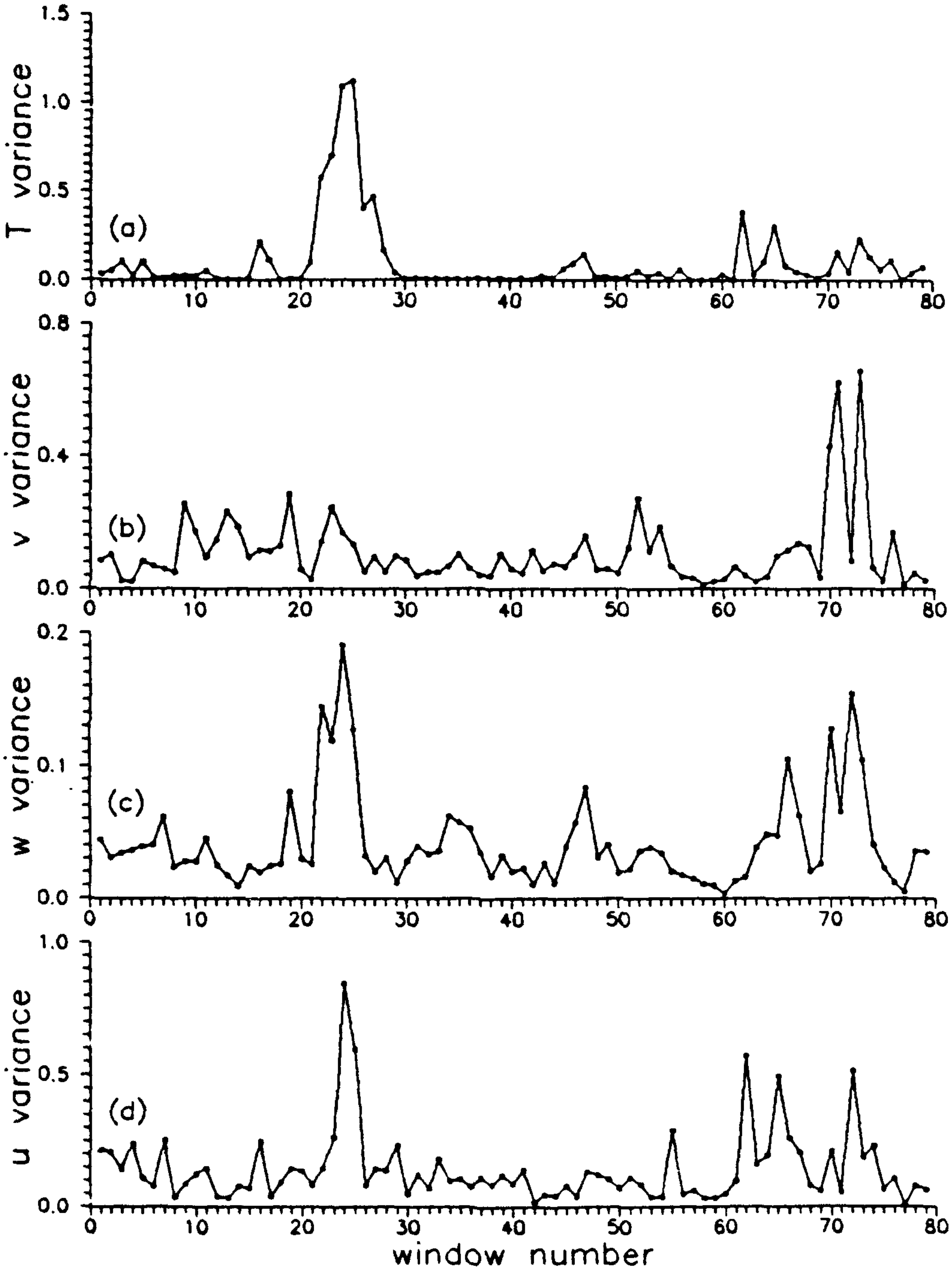

Figure 6 - Variances of: (a) T; (b) v; (c) w; (d) u.

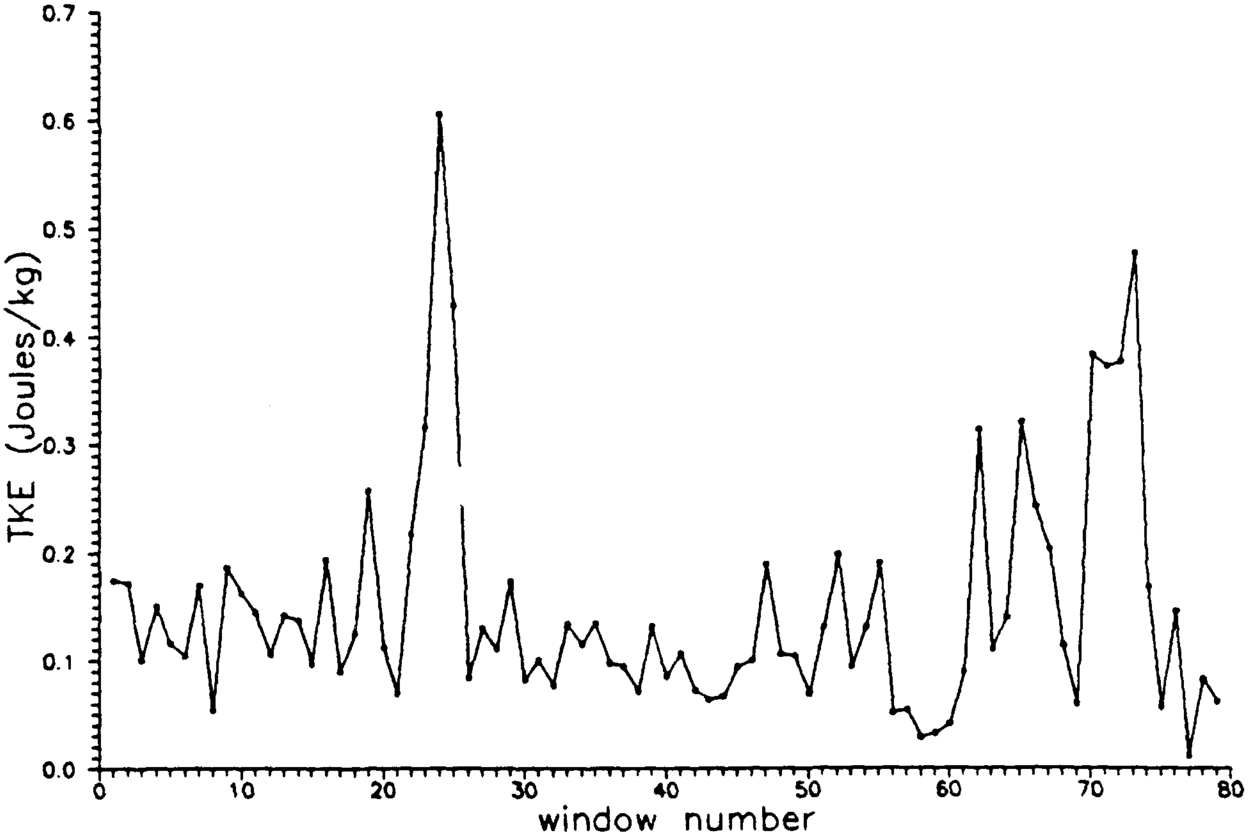

Figure 7 - Mean turbulent kinetic energy (TKE).

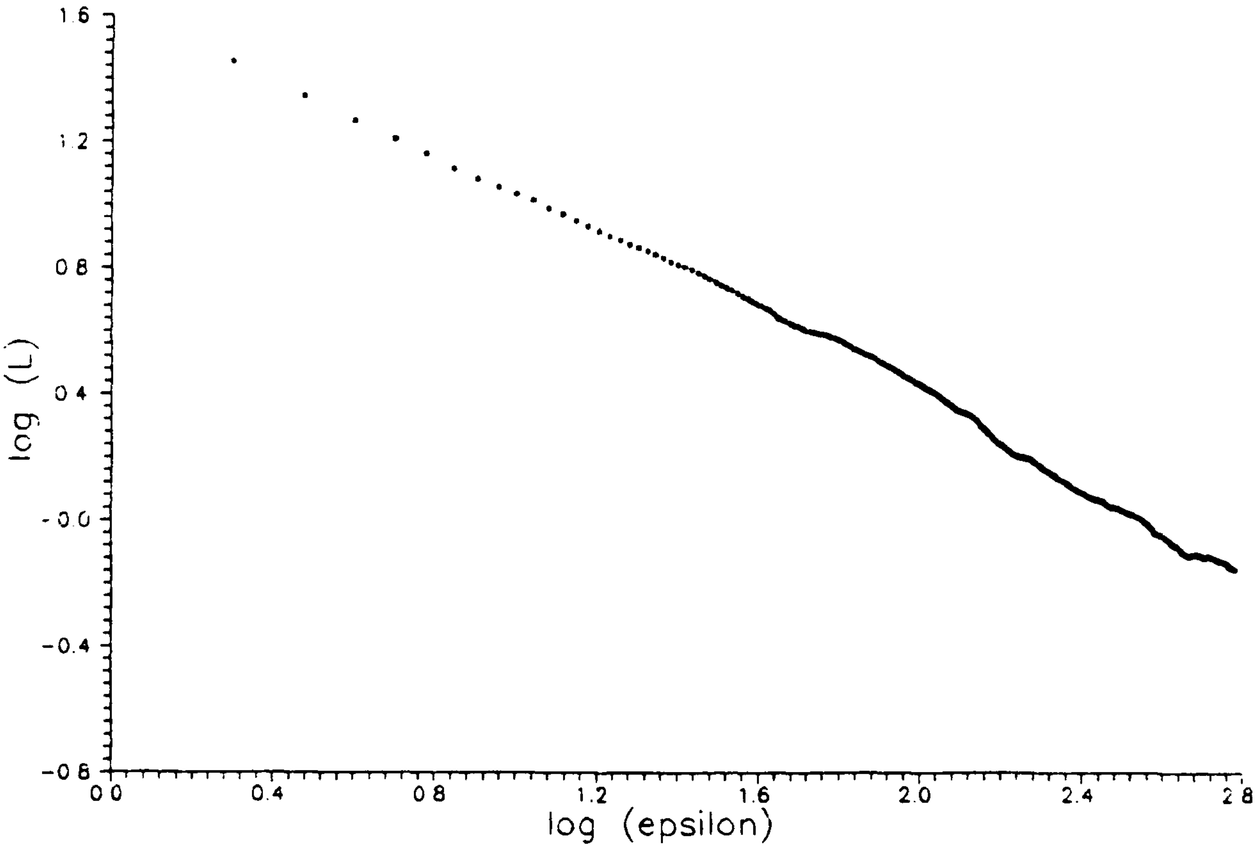

Figure 8 - Typical log-log plot from self-affine algorithm (D_A) from the temperature time series.

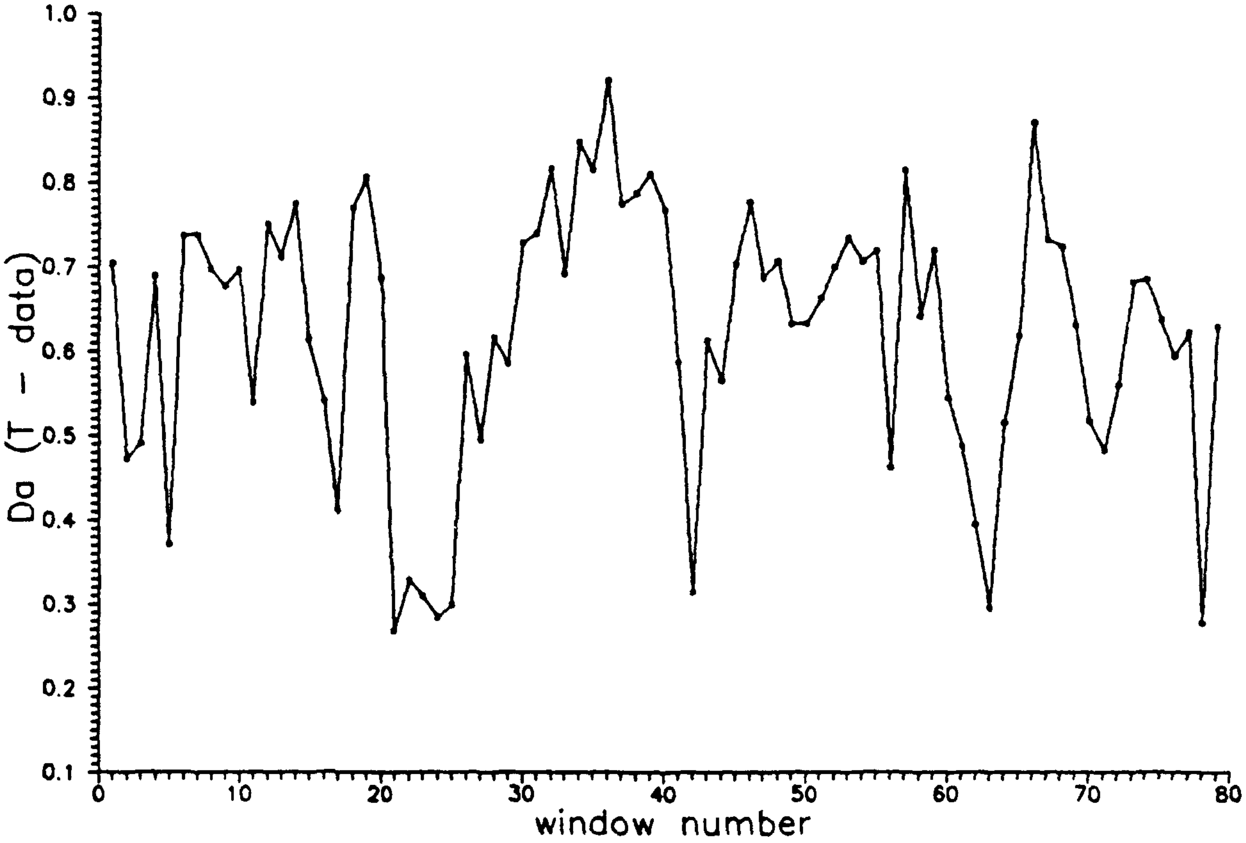

Figure 9 - D_A from temperature time series.

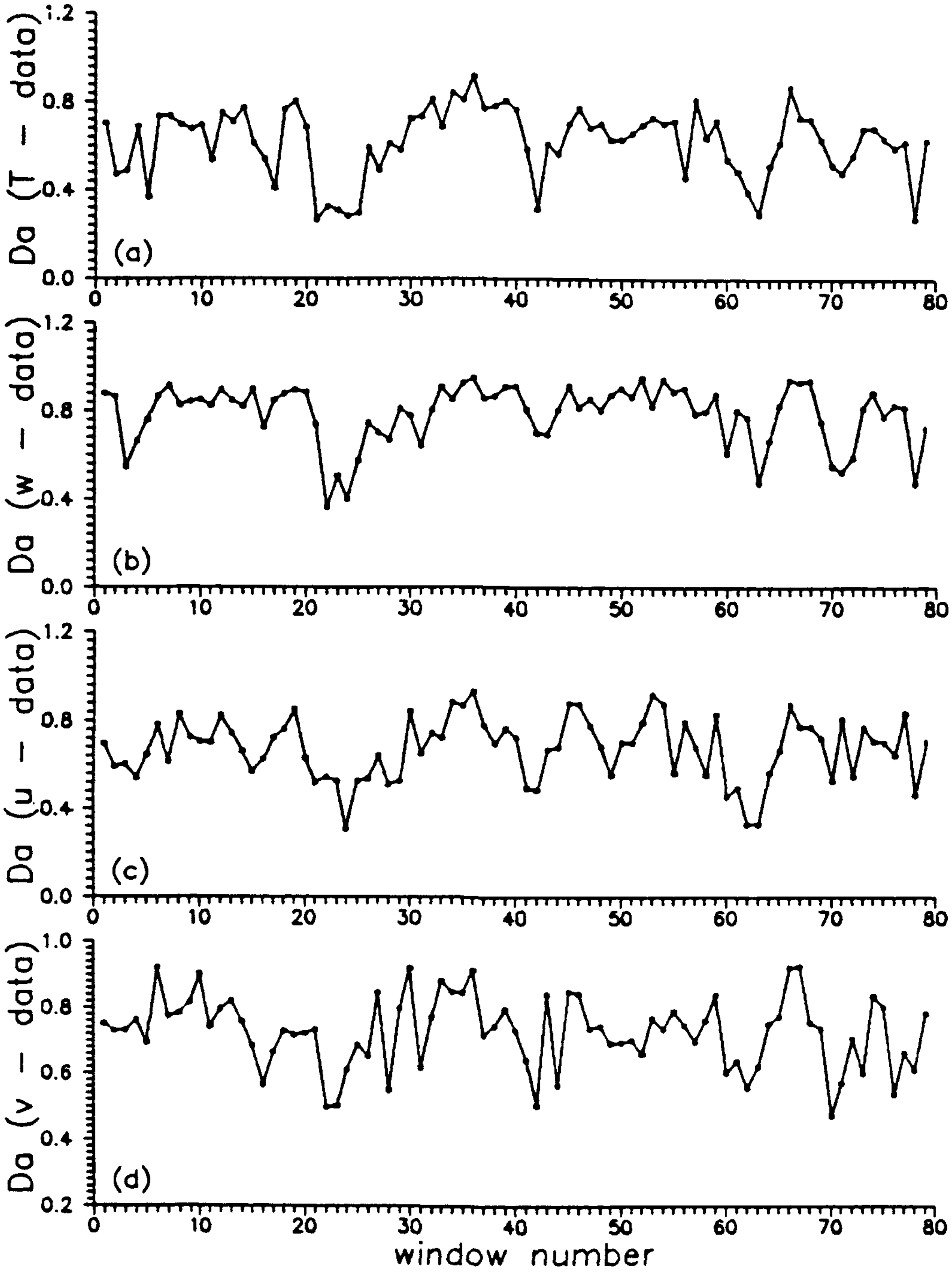

Figure 10 - D_A from: (a) T; (b) w; (c) u; and (d) v time series.

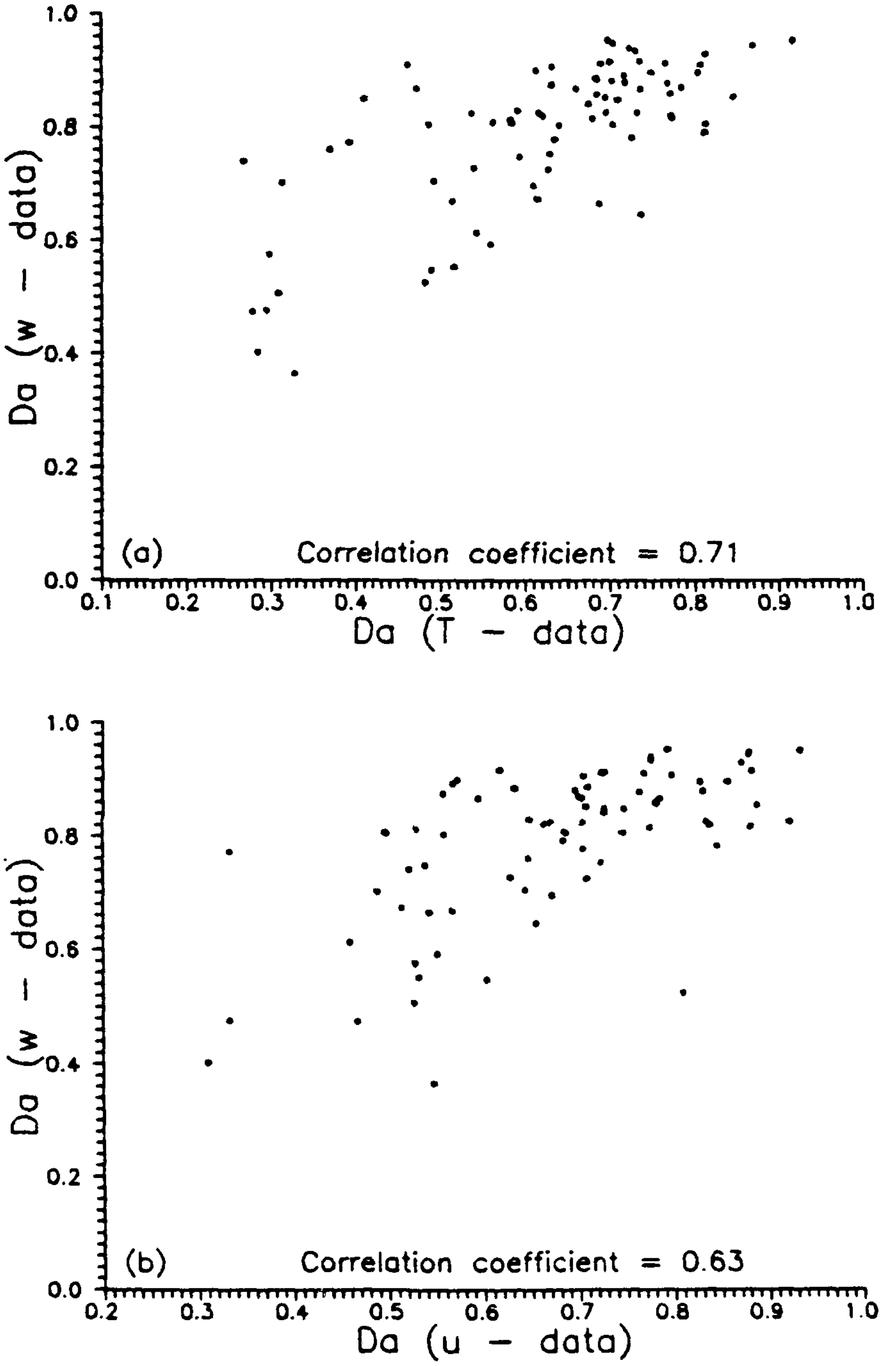

Figure 11 - Scattergrams of D_A from: (a) T vs. w; (b) u vs. w.

Thus, D_A seems to discriminate between "turbulence" (high D_A) and "wave" (low D_A) episodes. For nocturnal boundary layers this points to the possible use of $D_A \approx 0.35$ from temperature, or $D_A \approx 0.5$ from vertical velocity data as conditional sampling cut-off values to distinguish wave dominated periods from time series of hot-wire and sonic anemometer data, while retaining most of the real turbulence. However, more data containing both waves and turbulence must be analyzed before a firm value can be suggested. Different cut-off values may be appropriate for time series from other instruments, such as hot film, lidar, and cup anemometers having different amplitude ranges and time resolutions.

Though the following suggestion is untried as yet, note that D_A is large for "turbulence" but small for "waves", while the variances are large for both. So wave periods can be highlighted by scanning cotaneous windows with the combined operator, σ_w^2/D_A, while turbulence may be highlighted with the operator, $\sigma_w^2 D_A$.

All D_A values increase toward the end of the "wave", cotaneous with larger high frequency fluctuations in the T and w time series. This may indicate "wave-break", or wave-turbulence energy transfer. So D_A may also be useful in determining wave-break episodes, unlike other purely local measures such as variances or TKE. Waves may augment the local shear, thereby instigating instability, but they may also enhance TKE by increasing the buoyancy flux. Figure 12 shows a large increase in the non-phased averaged temperature flux and hence buoyancy flux during the latter part of the "wave" period, without a concommitant increase in the Reynolds stress portion of the TKE shear generation rate. R_B also plummets during "wave-break", and before one "turbulence" burst, but not prior to the other two "turbulence" episodes.

Cotaneous with the calm preceding these "turbulent" bursts, two of the local D_A minima occur just before the "turbulence" bursts and D_A maxima at windows 46 and 66. This is consistent with the proposal that local shear may gradually increase during periods of relative calm; but when such shear reaches an insupportable level, K-H instability may be initiated and rapidly grow into turbulence. This shear based initiation differs from the buoyancy based "wave" case above.

The highest D_A peak at window 36 bears more scrutiny, since it is cotaneous with a relatively calm appearing, low variance portion of the time series following the "wave" period. One possibility is that "wave" initiated turbulent mixing may persist for some time as intense but small scale turbulence, difficult to resolve by visual scanning alone. D_A may be a more acute discriminant than the eye itself.

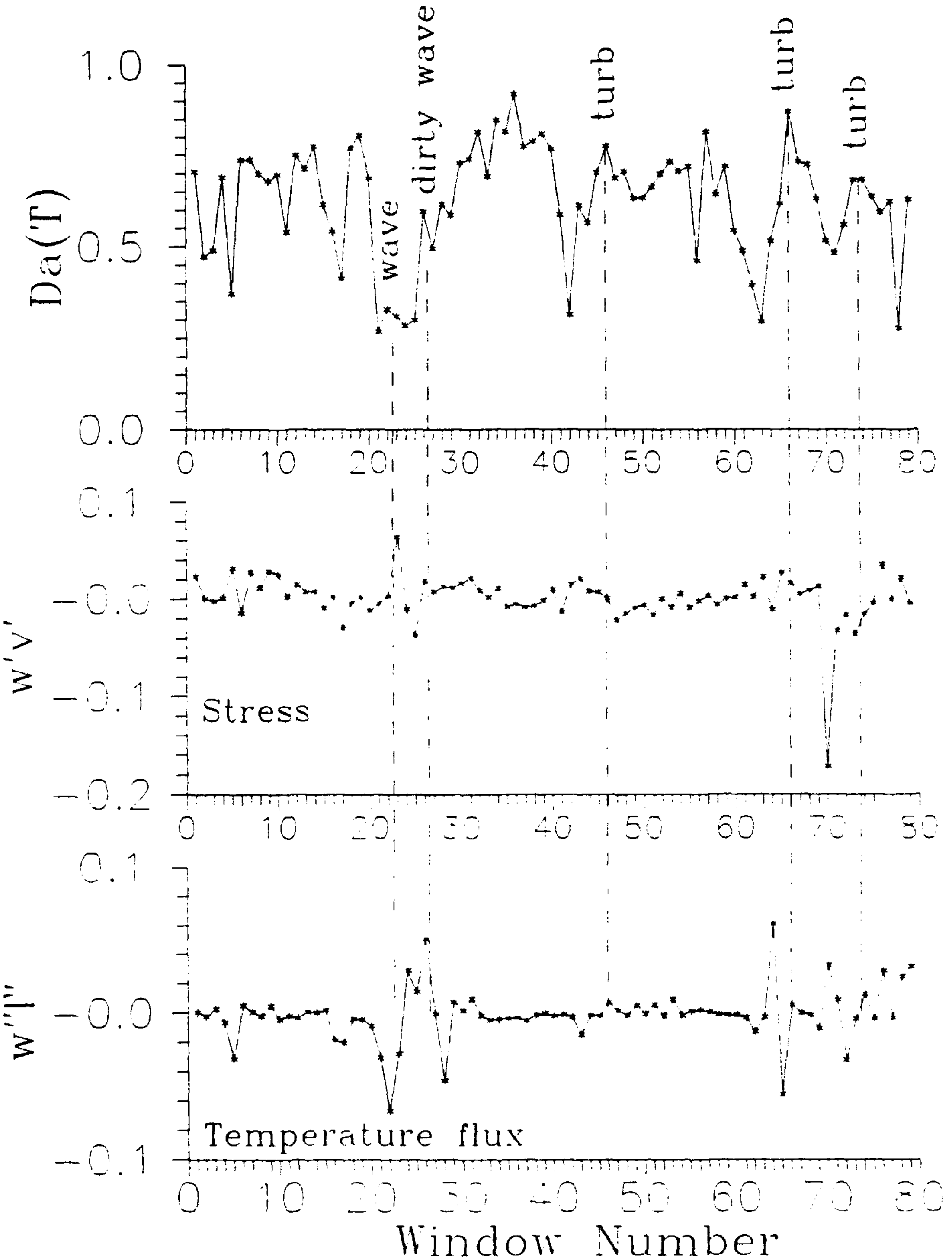

Fig. 12 - $D_A(T)$, stress, and temperature flux in Period A.

Alternatively, one might also suggest, due to the $1/\varepsilon$ weighting, that D_A is largely a scale separator which seems to distinguish between waves and turbulence only because turbulence in the stable boundary layer is generally smaller scale than waves. However, this does not explain the D_A minima also seen at windows: 5, 42, 56, 63, and 78, where the fluctuations seem to be small scale.

Since D_C, the self-similar, fractal dimension depends on the y to x-axis scaling ratio, we arbitrarily set .1 second = 100°C. As expected, D_C behaved differently from D_A, rising dramatically during the "wave" episode, and falling immediately after. This same behavior was observed during the "turbulent" episodes; thus, D_C did not distinguish between the "wave" and turbulence. Moreover, the long, ad hoc algorithm involved a dynamic range, $\varepsilon_i - \varepsilon_0$, smaller and more subjective than the limits used for D_A. For these reasons D_C does not seem useful as a wave/turbulence discriminant for time series and was not pursued further.

Figure 13a,b show Fourier spectra of the temperature data before and during the wave. Before taking the FFT, the data were linearly detrended and tapered. Despite such processing, the plots are quite noisy, showing only slight evidence of a spectral gap between the "wave" and higher frequency fluctuations. There is a decided increase in slope for the lower frequency components above 0.1 Hz which may indicate wave presence. However, the "turbulence" periods do not exhibit characteristics of any distinctive sort in the FFT plots, as shown in fig. 14a,b.

D_A also has a natural advantage over traditional spectral methods in that it assumes that the amplitude is constant over the time resolution in question. So D_A actually relies on local Chapeau basis functions rather than global basis functions, such as Fourier series, Bessel functions, etc. to obtain digitized amplitude differences. Thus, as illustrated in fig. 15, D_A has no problem in tracking large, nearly discontinuous jumps in amplitude, while FFTs require that linear combinations of wave numbers much higher than ε_i be found to both simulate such jumps and suppress fictitious ringing outside the area of the jump discontinuity.

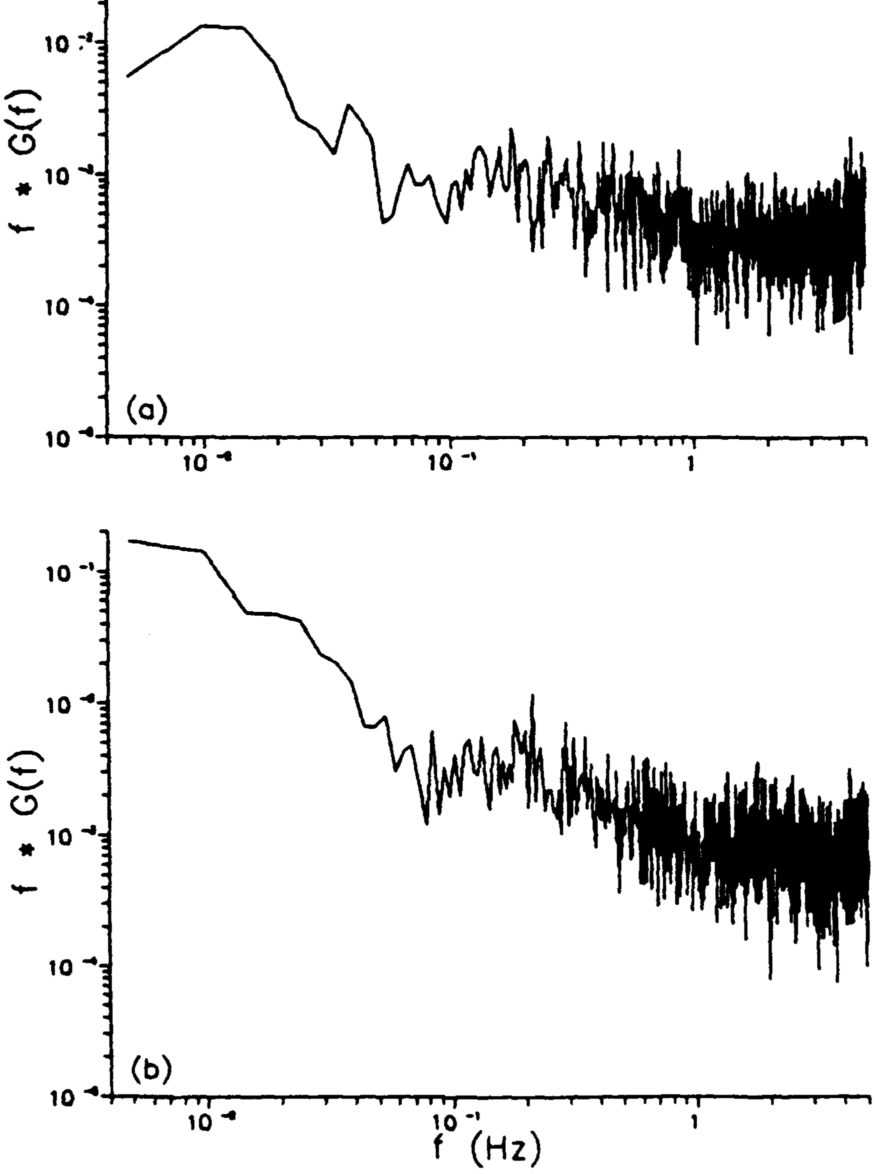

Figure 13 - FFT spectra from temperature time series: (a) before wave; and (b) during wave.

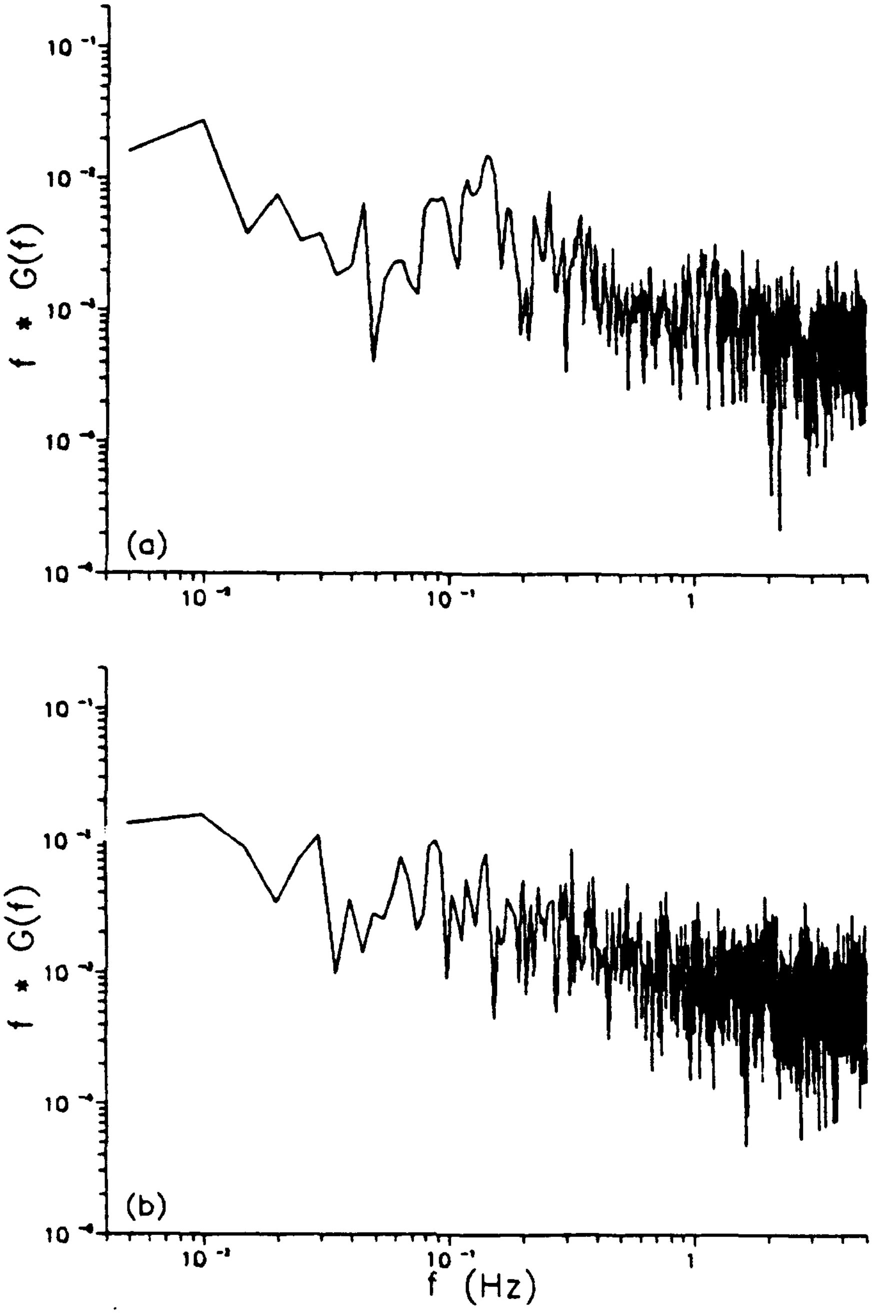

Figure 14 - FFT spectra from temperature time series: (a)before third turbulent episode; and (b) during turbulence.

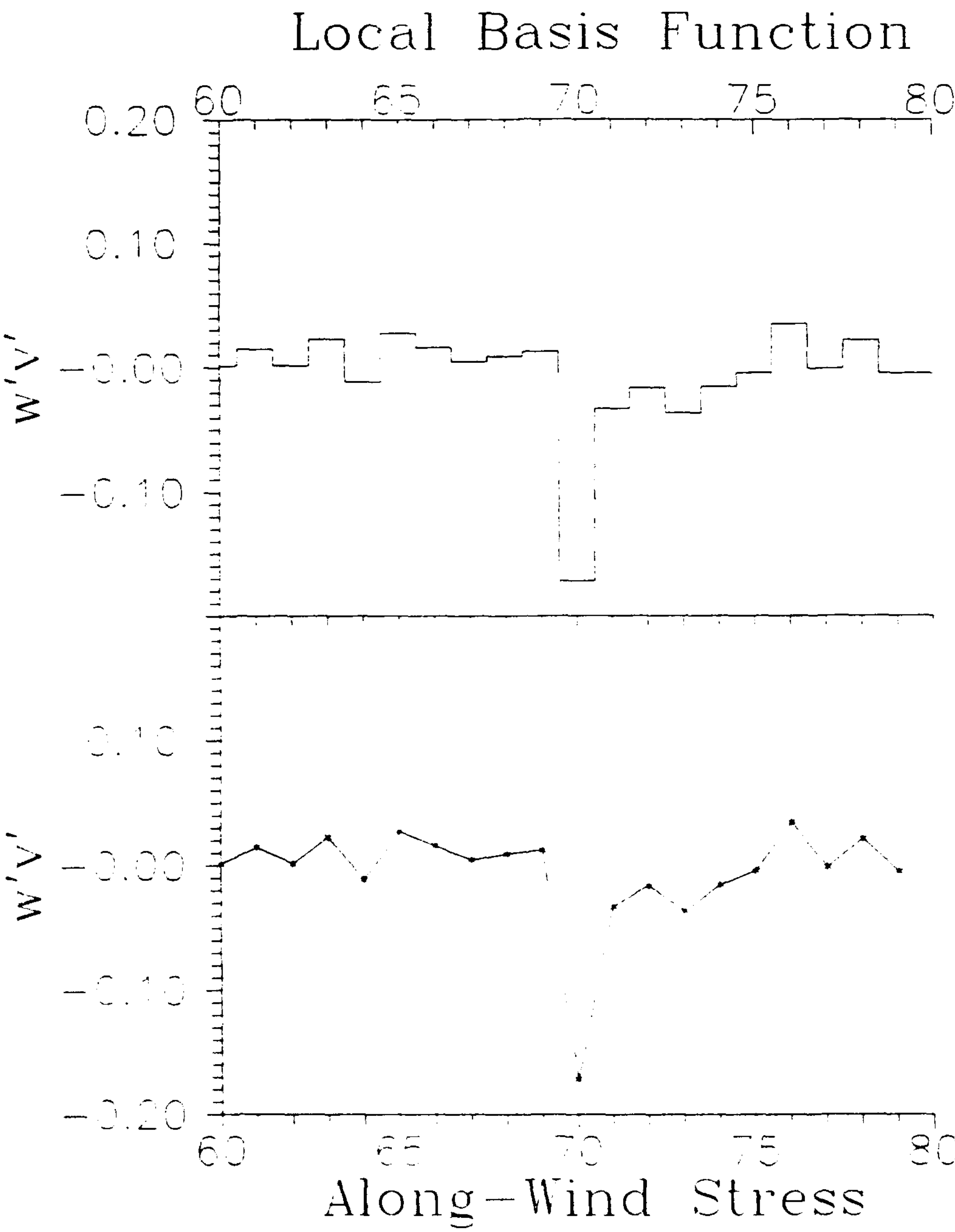

Figure 15 - Digital approximation of curve height at time resolution ϵ using Local Chapeau (top hat) basis functions.

B. Comparisons with bulk measures

Figures 16(a) and (b) show the temperature D_A compared with Brunt-Väisälä frequency (BVF). The BVF is highest during the "wave" when D_A is small. The three D_A minima at windows 42, 63, and 78 occur when the BVF is at or near a local maxima, consistent with the fact that a higher BVF (more stable) will tend to dampen turbulence. Also, most of the D_A maxima occur when the BVF is either decreasing or at a minimum, which indicates a less stable, more turbulent atmosphere. But high BVF values occurred during both "wave" and "turbulence" periods, so BVF cannot be used to resolve the two. Figure 16(c) shows a scatter plot of the temperature D_A versus BVF, which indicates a weak negative correlation.

Figure 17 shows another weak, but positive, correlation between D_A and l_B, the buoyancy length scale. The correlation is highest during the "wave" episode, when l_B drops rapidly, simultaneous with a rapid drop in D_A. After the "wave", D_A and l_B both rise. The u and T variances and BVF show local maxima at window 62, while the u and w variances and l_B show local minima. The temperature time series shows a rapid monotonic temperature fall. l_B does not seem to distinguish between "wave" and turbulence. All such episodes show moderate l_B on the order of 8-12 meters. Since the BVF is in the denominator of l_B, l_B peaks during windows 18-20, and 35-40 when the BVF is low. This seems to occur when the temperature time series is relatively calm. Thus, large l_B does not seem to correlate with turbulence, and does not seem to be a good measure of dominant eddy scale, as some have suggested (Stull, ibid).

Comparison of D_A with R_B in fig. 18 shows little correlation except during the "wave" when R_B rises dramatically, indicating increased stability. None of the bulk measures seem to reliably distinguish between "wave" and "turbulence" episodes. Note however, that high correlations between D_A and BVF, R_B, or l_B may not be reasonable, since D_A is a local measure, whereas the latter three are bulk measurements from widely vertically separated sensors. Higher correlations might be expected, if more local measurements of $\Delta\theta$ and Δu were available. However, this capability is not currently present on the BAO tower or similar facilities.

The wave/turbulence energy transfer during windows 25-28 may initially blend the potential temperatures across levels 3 to 5 (see Fig. 19), resulting in high l_B and low BVF after window 35. This is consistent with the local maxima in the w and v variances around window 35. However, again the large D_A maxima in window 35 of the u, v, w, and T traces may suggest continued turbulent blending, principally at smaller scales, even after the level 4 and 5 potential temperatures have become well-mixed.

Though not suggested by our data, it is still possible that such smaller scale blending is unduly accentuated, since D_A is normalized by $1/\varepsilon^n$, where n was assumed to equal unity. For inertial eddy cascade processes, n may indeed be less than unity. As a first guess, since the turbulence energy spectrum tends to have a -2/3 slope in the inertial subrange, one might expect the turbulence velocity spectrum to have a -1/3 slope. In that case, perhaps the correct self-affinity factor for inertial subrange turbulence should be n = 1/3. So to modify D_A one would first have to modify the integrand in II.14 somehow to retain the units of pure amplitude for $L(\varepsilon)$.

Secondly, in practice the inertial subrange scaling assumption is not entirely viable. The BAO data resolution is 0.1 seconds, which enters the dissipation range where the spectral energy slopes are much higher. To eliminate contributions from this range, the inner scale cutoff would have to be at longer times, thus narrowing the dynamic range over which D_A is computed. This may be possible for convective data, since a longer window must be used to capture fluctuations due to boundary layer scale eddies.

Thirdly, stability also tends to compress the vertical extent of an eddy. Thus, inertial subrange turbulence may not have a -⅔ slope in the energy spectrum, as in self-similar turbulence. That is, there will be less energy in the larger scales. Mahrt and Gamage (1987) have studied vertical/horizontal velocity aspect ratios for structure functions as a function of stability. However, their stability categories were not well defined by R_i or other measures.

In light of these difficulties and lack of supporting data, we retain the present self-affine operator, D_A, and note that it appears to be the first potentially operationally useful wave/turbulence discriminant. It may also be useful as a fast pre-processor to quickly locate intermittent wave or turbulence periods for more detailed phase averaged studies.

As an extension of this study, another potential use for D_A is as a general measure of the degree of chaos, applied to systems ranging from pure waves and limit cycles, through standard chaotic systems such as the Henon, Poincare, and Lorenz maps, as well as transitional turbulence, and turbulence displaying extended inertial subranges. One effort has begun to test D_A on a set of differential equations which describe coupled harmonic oscillators. By eye the degree of chaos expressed in each oscillator's motion seems to increase or decrease monotonically along the oscillator lattice. An adequate measure this chaos has not been shown as yet.

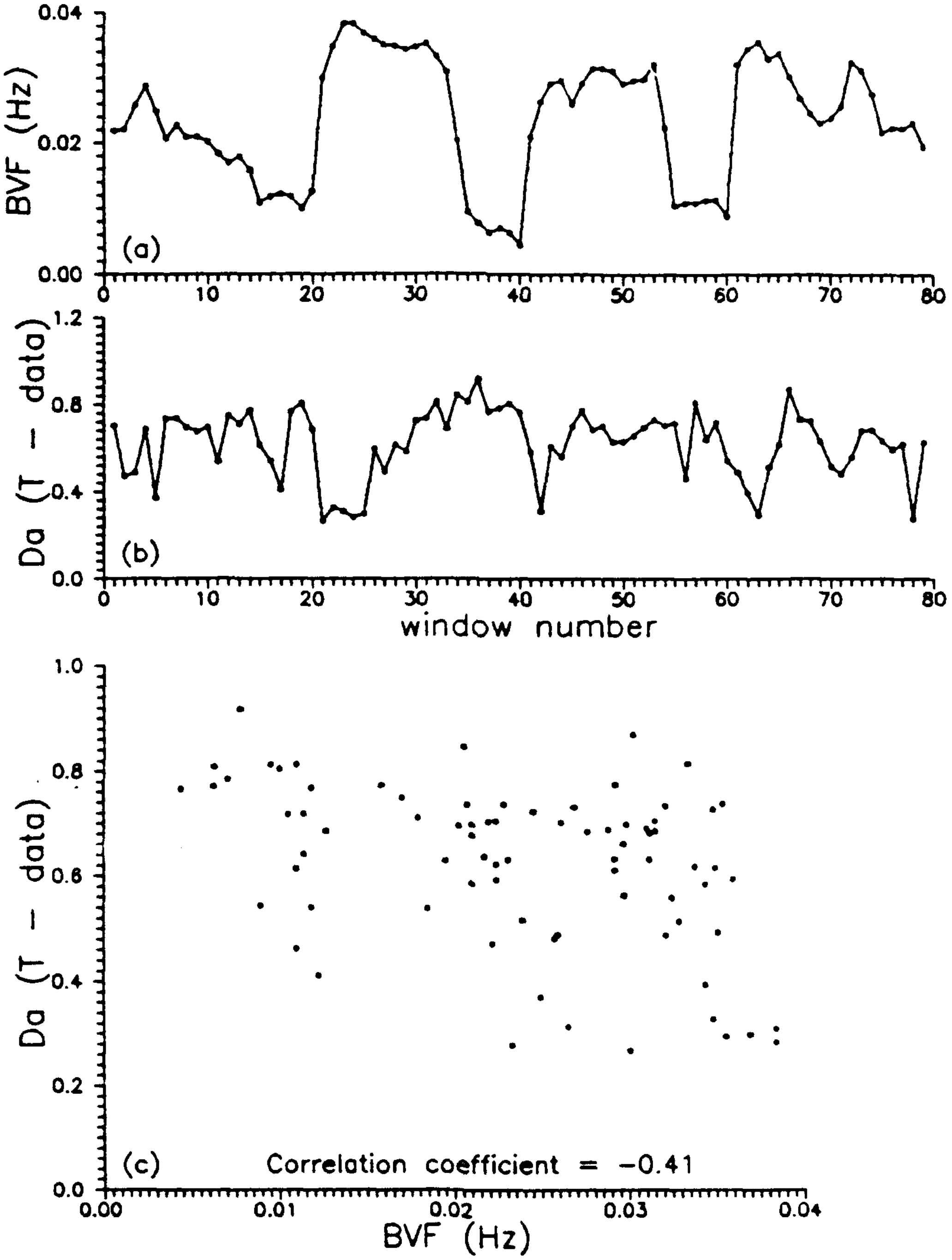

Figure 16 - (a) BVF; (b) D_A from T time series; (c) D_A vs. BVF.

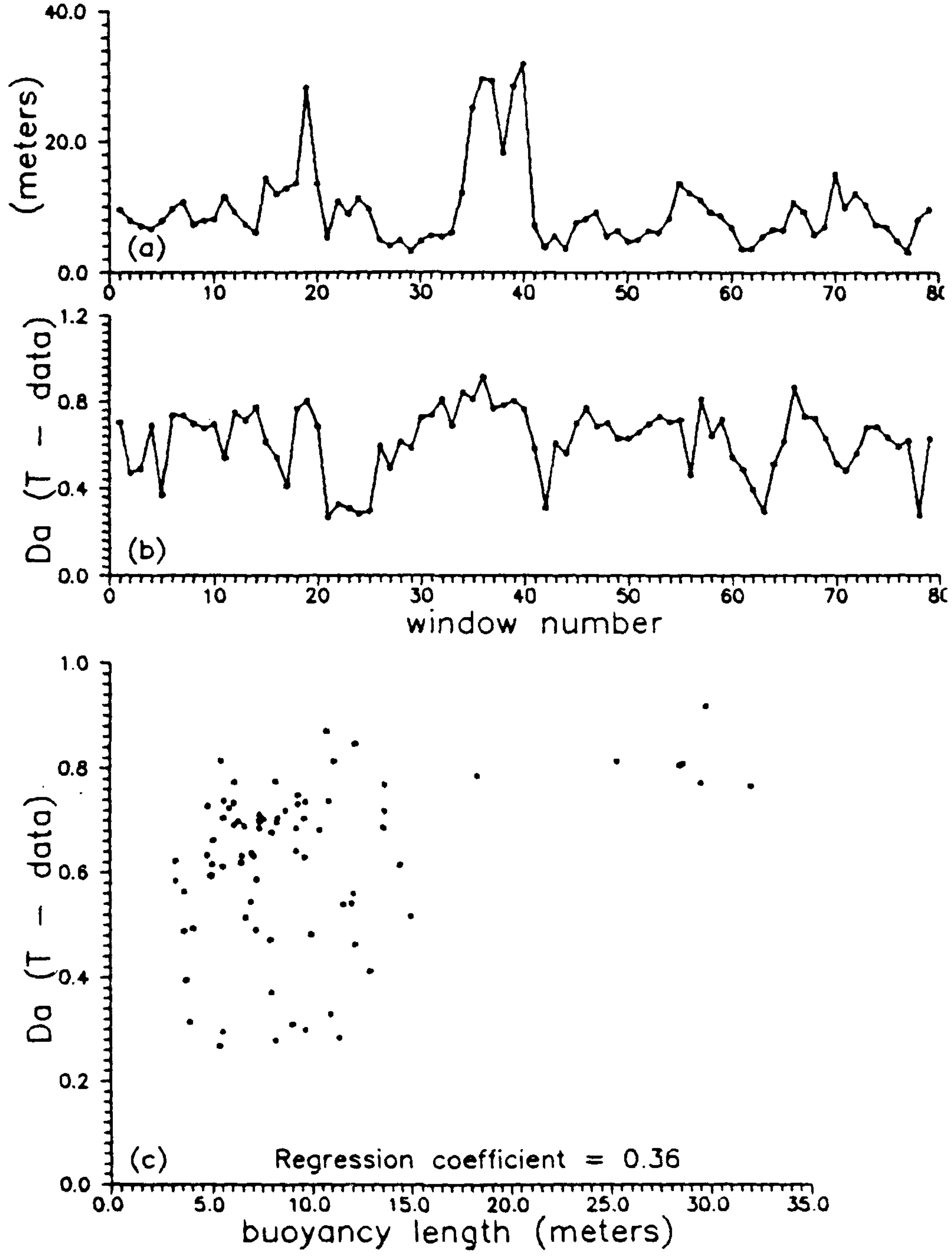

Figure 17 - (a) l_B; (b) D_A from T time series; (c) D_A vs. l_B.

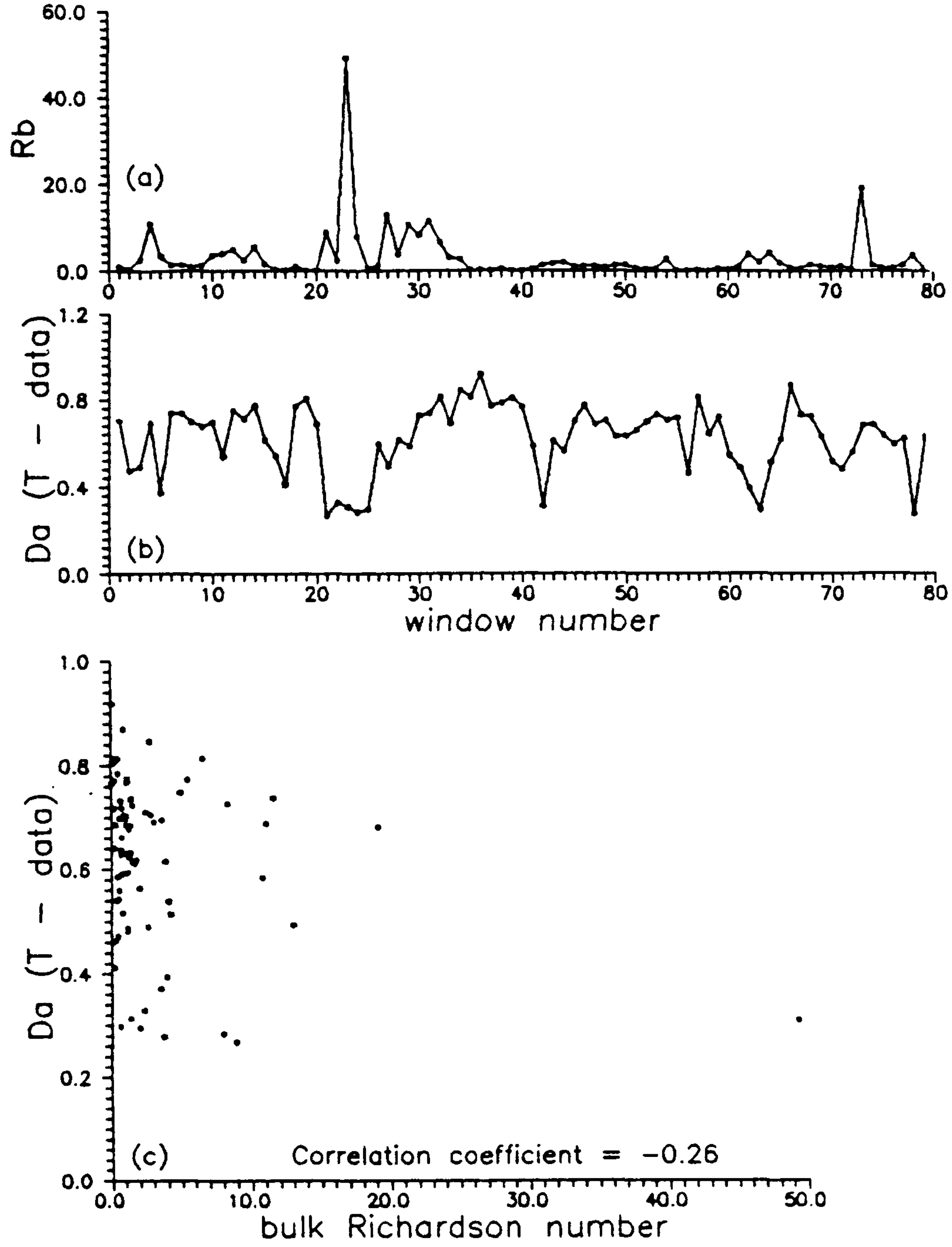

Figure 18 - (a) R_B; (b) D_A from T time series; (c) D_A vs. R_B.

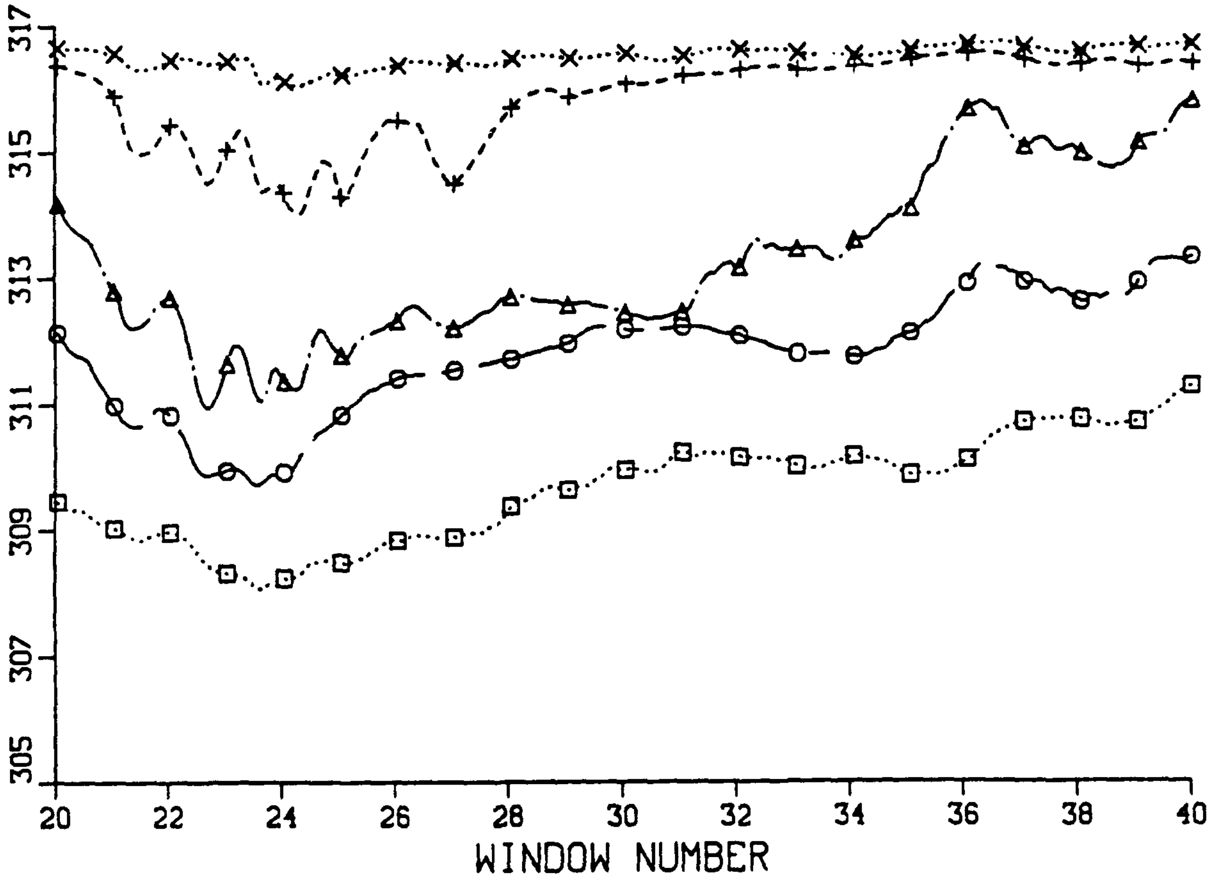

Figure 19 - θ profile (°K) during and after wave.
□ - 10 m; ○ - 22 m; △ - 50 m; + - 100 m; x - 150 m

"turbulence" episodes.

In terms of computational efficiency D_A does not require that coefficients be determined for linear combinations of wave frequencies to approximate moments of the time series amplitude, i.e., no transform is needed. Moreover, since the slopes used to determine D_A seem well-behaved, perhaps sufficiently accurate values of D_A may be determined by computing $L(\varepsilon)$ only at the inner and outer time resolutions. This would render D_A computations orders of magnitude faster than FFTs. Moreover, FFTs tend to treat finite wave trains, i.e., discontinuities quite poorly. D_A avoids this problem because it involves local Chapeau basis functions, rather than global transcendental or other basis functions. This makes D_A a potentially suitable analysis tool for turbulence intermittency and coherent structures in general.

D_A also shows promise in resolving wave-turbulence energy transfers, or "wave-break" events. We suspect that "turbulence" following the "wave" period studied may have been initiated by growing positive buoyancy flux, while other "turbulence" episodes may have relied more on shear generation of TKE. However, correlations between D_A and "wave-break" should be tested in more detail, perhaps with the Gossard (ibid) data set which involved vertical carriage traverses along the BAO tower, wherein local values of R_i were measured. Ultimately, one would like to establish D_A as a function of local stability, so that D_A turbulence cut-off values could be associated with critical R_i.

Tentatively, we interpret the anomalous temperature D_A peak following the "wave" period as indicative of intense but small scale turbulence, not easily resolved by visually scanning the time series trace. Alternatively, due to the $1/\varepsilon$ self-affine normalization, D_A may act as simply a "scale" discriminator rather than a wave/turbulence discriminator. However, D_A minima were also found during periods where visual scanning suggested low turbulence levels, not consistent with the latter interpretation. Further investigation to test D_A on convective data is suggested to explore this possibility. Proceeding in the other direction as well, D_A should be tested on systems which lie between the wave and limit cycle regimes and turbulent systems displaying extended inertial subranges, such as the Henon, Poincare, Lorenz, and other standard chaotic attractors, to see if D_A can distinguish degrees of chaos in general. An immediate effort is underway to test D_A on differential equations which describe coupled harmonic oscillators. To the eye in certain modes each oscillator along the lattice seems to display increasingly chaotic motion. An adequate measure of the this chaos has not been demonstrated as yet.

An $n = 1/3$ self-affine scaling factor for ε is discussed as possibly more suitable for turbulence, though this would require modification of the integrand in II.14 to avoid making $L(\varepsilon)$ also a function of time.

IV. SUMMARY AND CONCLUSIONS

Time series of T, u, v, and w from a stable atmospheric boundary layer were examined using fractal techniques. The time series were taken from 10Hz sonic anemometer and hot wire data at a height of 100 meters on the mast at the Boulder Atmospheric Observatory (BAO). The time series featured a probably terrain induced gravity "wave" period, as well as several periods of intermittent turbulence.

Both self-similar fractal dimension, D_C, and self-affine fractal dimension, D_A, were explored in the analysis. The latter was clearly superior in practice as well as principle. D_A was the only measure among the eight (five local and three bulk) studied which seemed to distinguish the "wave" from "turbulent" episodes, reaching minima during "wave" and maxima during "turbulence".

Since D_A is a local measure, this implies that tower data from a single fast response sensor can be used for wave/turbulence discrimination, while phase averaging requires extensive numerical processing and microbarograph array data as well. Most tower sites are not equipped with microbarograph arrays.

Phase averaging also requires that the wave period be known prior to analysis, otherwise the wave and turbulent components cannot be distinguished. D_A also requires an estimate of the minimum expected wave period, λ_m, to specify ε_0, the outer scale for the slope. However, the required precision is perhaps a factor of two, much lower than is needed for phase averaging. For λ_m we note that nocturnal atmospheric boundary layer gravity waves have typical periods in the range 100 - 300 seconds.

From the limited results we tentatively suggest a conditional sampling cutoff value, $D_A \approx 0.35$, to remove wave data from a hot wire temperature time series. However, more data needs to be analyzed to establish a firmer value. Since σ_w^2 peaks during both waves and turbulence, dividing D_A by σ_w^2 should highlight the wave periods. Similarly, turbulence should be highlighted by multiplying D_A by σ_w^2.

Correlations between D_A and various bulk measures of stability were investigated, with weak correlations ($r \leq .41$) found with Brunt-Väisälä frequency (BVF) and buoyancy length (l_B), and little correlation with bulk Richardson number (R_B). The issue of inherently low correlations between local and bulk measures was discussed.

Other possible parameters for distinguishing waves and turbulence were investigated. Turbulent kinetic energy (TKE) proved less than useful, since it included wave energy. Fast Fourier Transform spectra were able to resolve the "wave" event as a change in slope at low frequency, but no distinguishing features were found for the

15. Mahrt, L., and N. Gamage, 1987: Observations of turbulence in stratified flow. *J. Atmos. Sci.*, **44**, 1106-1121.

16. Mandelbrot, B. B., 1977: *The fractal geometry of nature*, W. H. Freeman and Company.

17. -----, 1985: Self-affine fractals and fractal dimension. *Physica Scripta.*, **32**, 257-260.

18. McHardy, I., and B. Czerny, 1987: Fractal X-ray time variability and spectral invariance of the Seyfert galaxy NGC5506. *Nature*, **325**, 696-698.

19. Moon, F. C., 1987: *Chaotic vibrations*, John Wiley and Sons.

20. Nai-Ping, L., 1983: Wave and turbulence structure in a disturbed nocturnal inversion. *Bound.-Layer Meteor.*, **26**, 141-155.

21. Packard, N. H., J. P. Crutchfield, J. D. Farmer, and R. S. Shaw, 1980: Geometry from a time series. *Phys. Rev. Lett.*, **45**, 712-716.

22. Pawelzik, K., and H. G. Schuster, 1987: Generalized dimensions and entropies from a measured time series. *Phys. Rev. A*, **35**, 481-484.

23. Presad, R. R., and K. R. Sreenivasan, 1990: The measurement and interpretation of fractal dimensions of the scalar interface in turbulent flows. *Phys. Fluids A*, **2**, 792-807.

24. Richardson, L. F., 1922: *Weather prediction by numerical process.*, Cambridge Univ. Press.

25. Schertzer, D., and S. Lovejoy, 1984: in *Turbulence and chaotic phenomena in fluids.*, edited by T. Tatsumi, Elsevier Science Publishers B.V.

26. Sreenivasan, K. R., and C. Meneveau, 1986: The fractal facets of turbulence. *J. Fluid Mech.*, **173**, 357-386.

27. Stull, R. B., 1988: *An Introduction to Boundary Layer Meteorology*, Kluwar Academic Publishers.

REFERENCES

1. Atlas, D., and J. I. Metcalf, 1970: The birth of "CAT" and microscale turbulence. *J. Atmos. Sci., 27*, 903-913.

2. Beyer, W. H., 1987: *CRC standard mathematical tables.*, CRC Press.

3. Carter, P. H., R. Cawley, A. L. Licht, and J. A. Yorke, 1986: in *Dimension and entropies in chaotic systems.*, edited by G. Mayer-Kress, Springer-Verlag.

4. Caughey, S. J., 1977: Boundary-layer turbulence spectra in stable conditions. *Bound.-Layer Meteor.*, **11**, 3-14.

5 -----, and C. J. Readings, 1975: An observation of waves and turbulence in the Earth's boundary layer. *Bound.-Layer Meteor.*, **9**, 279-296.

6. Feigenbaum, M.J., 1980: Universal behavior in nonlinear systems. *Los Alamos Sci. Lab.* 1, 1, 4-27.

7. Finnigan, J. J., 1988: Kinetic energy transfer between internal gravity waves and turbulence. *J. Atmos. Sci.*, **45**, 486-505.

8. Gossard, E. E., J. E. Gaynor, R. J. Zamora, and W. D. Neff, 1985: Finestructure of elevated stable layers observed by sounder and in situ tower sensors. *J. Atmos. Sci.*, **42**, 2156-2169.

9. Grebogi, C., E. Ott, and J. Yorke, 1987: Chaos, strange attractors, and fractal basin boundaries in nonlinear dynamics. *Science.*, **238**, 632-638.

10. Hines, C. O., 1988: Generation of turbulence by atmospheric gravity waves. *J. Atmos. Sci.,* **45**, 1269-1278.

11. Hunt, J. C. R., 1980: in *Workshop on the Planetary Boundary Layer.*, edited by J. C. Wyngaard, Amer. Meteor. Soc.

12. Kaimal, J. C., and J. E. Gaynor, 1983: The Boulder Atmospheric Observatory. *J. Appl. Meteor.,* **22**, 863-880.

13. Kamada, R.F., 1988: A Fractal interfacial entrainment model for dry convective boundary layers. Part I: Model description. J. Atmos. Sci., *J. Atmos. Sci.* 45, 17, 2365-2374.

14. Kamada, R.F., 1988: A Fractal interfacial entrainment model for dry convective boundary layers. Part II: Discussion of model behavior and comparison with other models. *J. Atmos. Sci.* 45, 17, 2375-2383.

DISTRIBUTION LIST

		No.copies
1.	Defense Technical Information Center Cameron Station Alexandria, VA 22314	2
2.	Dudley Knox Library Code 52 Naval Postgraduate School Monterey, CA 93943-5000	2
3.	Director of Research (08) Naval Postgraduate School Monterey, CA 93943-5000	1
4.	Dept. of Physics (PH) Naval Postgraduate School Monterey, CA 93943-5000	2
5.	Chairman (Code MR/Hy) Department of Meteorology Naval Postgraduate School Monterey, CA 93943-5000	1
6.	Dr. Ray Kamada/061kd Naval Postgraduate School Monterey, CA 93943-5100	11
7.	Ken Davidson (Code MR/Ds) Department of Meteorology Naval Postgraduate School Monterey, CA 93943-5000	1
8	Roland Garwood (Code OC/gd) Department of Oceanography Naval Postgraduate School Monterey, CA 93943-5000	1
9.	Teddy Holt (Code MR/Ht) Department of Meteorology Naval Postgraduate School Monterey, CA 93943-5000	1
10.	Alex DeCaria 825 E. Adams st. Layton, UT 84041	2
11.	Capt. David Struck (SSD/CLGR) Los Angeles AFB Los Angeles, CA 90009-2960	1

12.	Prof. Gordon Schacher Dean of Faculty and Graduate Studies Naval Postgraduate School Monterey, CA 93943-5100	1
13.	Capt. Mike Moss (AFESC/RDVS) Tyndall AFB, FL 32403-6001	1
14.	Lt. Col. Stephen Pryor (730 SPW) Vandenberg AFB, CA 93437-5000	1
15.	Mr. Steve Sambol (730 SPW/DOW) Vandenberg AFB, CA 93437-5000	1
16.	Mr. Randy Nyman ACTA Vandenberg AFB, CA 93437-5000	1
17.	Dr. Don Ermak Lawrence Livermore National Lab P.O. Box 808, L-262 Livermore, CA 94551	1
18.	Mr. Bruce Kunkel (PL/GPAA) Hanscom AFB, MA 01730-5000	1
19.	Mr. Bill Boyd (45 WS/WER) Patrick AFB, FL 32925-5000	1
20.	Mr. John Edwards SSD/DEV Los Angeles, AFB, CA 90009-2960	1
21.	Mr. Larry Mendenhall Geodynamics Corp. 21171 Western Ave Suite 100 Torrence, CA 90501	1
22.	Mr. Bart Lundblad (Aerospace/El Segundo) PO Box 92957 Los Angeles, CA 90009	1
23.	Mr. Jose Caraballo NASA Industrial Safety/RT-SOE KSC, Florida 39899	1
24.	Mr. Jan Zysko NASA PM-PCO-4 KSC, Florida 39899	1

25. Dr. Tetsuji Yamada 1
Yamada Science and Art
147 Monterey Bay Dr. S.
Los Alamos, NM 87544

26. Dr. D. Pepper 1
5301 N. Commerce #A
Moorpark, CA 93021

27. Dr. Roger Gibbs 1
Naval Surface Warfare Center
Dahlgren, Virginia 22448-5000

28. Dr. Kenneth Moe 1
USAF Space Division
Box 92960 World Way
Los Angeles, CA 90009-2960

29. Dr. Torben Mikkelsen 1
Meteorologie und Vind Energie Dept.
RISO National Laboratory
DK-4000
Roskilde, Denmark

30. Dr. Neals Otto Jensen 1
Meteorologie und Vind Energie Dept.
RISO National Laboratory
DK-4000
Roskilde, Denmark

31. Dr. John C. Wyngaard 1
Dept. of Meteorology
Pennsylvania State University
University Park, PA 16802

32. Dr. Gary Geernert 1
ONR, Office of the Chief of Naval Operations
Arlington, VA 22217

33. Dr. Ted Tsui 1
Naval Research Laboratory
Monterey, CA 93943-5006

34. Dr. Steve Burke 1
Naval Research Laboratory
Monterey, CA 93943-5006

35. Dr. Paul Gudiksen 1
Lawrence Livermore National Lab
P.O. Box 808, L-262
Livermore, CA 94551